Available online at www.sciencedirect.com

ScienceDirect

Physics of the Earth and Planetary Interiors 163 (2007) 209–232

PHYSICS OF THE EARTH AND PLANETARY INTERIORS

www.elsevier.com/locate/pepi

Physical controls of magmatic productivity at Pacific-type convergent margins: Numerical modelling

Weronika Gorczyk[a,*], Arne P. Willner[b], Taras V. Gerya[a], James A.D. Connolly[a], Jean-Pierre Burg[a]

[a] *Department of Geosciences, Swiss Federal Institute of Technology (ETH-Zürich), CH-8092 Zurich, Switzerland*
[b] *Institute of Geology, Mineralogy and Geophysics, Ruhr University Bochum, 44870 Bochum, Germany*

Received 21 January 2007; received in revised form 17 May 2007

Abstract

We use a coupled petrological–thermomechanical model of subduction with spontaneous slab bending to investigate magmatic productivity at active continental margins. The model is designed to simulate fossil Pacific-type margins that have a broad well-developed fore-arc accretionary wedge system. The degree of plate coupling strongly depends on the dimensionless ratio (R_{H_2O}) between the plate convergence rate and the water propagation velocity. Delamination of the slab from the overriding plate followed by trench retreat is common for models with relatively slow convergence rates ($R_{H_2O} < 4$). In contrast, higher convergence rates ($R_{H_2O} > 4$) result in continuous plate coupling. The slab bending curvature increases with the length of the subducted plate. Periodic variations of the slab angle with time are observed at the later stages of subduction and become more conspicuous with depth. These variations are favoured by slower subduction rates and stronger oceanic crust.

Two fundamentally different regimes of melt productivity are observed in numerical experiments and correlated with natural observations: (1) during continuous convergence with coupled plates (as in the Late Paleozoic margin of central Chile) the largest melt productivity occurs at the onset of subduction due to temporary steepening of the slab, productivity then decays rapidly with time due to flattening of the slab inclination angle, thereby precluding further formation of partially molten mantle wedge plumes. (2) Highest melt productivity is obtained in simulations associated with slab delamination and trench retreat. As a result an extension occurs with decoupling of plates that finally leads to the formation of a pronounced back-arc basin (similar to the Mesozoic margin of southernmost Chile). In this case melt production increases with time due to stabilization of slab inclination associated with upward asthenospheric mantle flow toward the spreading centre, thereby favouring the generation of hydrous partially molten plumes from the slab.

Keywords: Numerical modelling; Active margin; Mantle wedge melting; Slab retreat; Back-arc spreading; Magmatic productivity

1. Introduction

Convergent plate margins are presently the dominant sites on Earth for crustal growth, destruction and recycling as well as mass transfer between the crust and the mantle. Mass transfer and interaction between crust and mantle at convergent margins occurs by tectonic as well as magmatic processes. Aspects of cyclic mass flow at active continental margins have been studied by numerical experiments (e.g., Gerya et al., 2006, 2002; Sobolev and Babeyko, 2005) and analogue simulations (e.g., Gutscher et al., 1998; Kukowski et al., 2002). Water transport and related metamorphic and

---

[*] Corresponding author. Tel.: +41 44 632 8817; fax: +41 44 632 1030.
E-mail address: weronika.gorczyk@erdw.ethz.ch (W. Gorczyk).

0031-9201/$ – see front matter © 2007 Elsevier B.V. All rights reserved.
doi:10.1016/j.pepi.2007.05.010

magmatic processes have recently been addressed in a variety of studies (e.g., Arcay et al., 2005; Iwamori et al., 2007; Rupke et al., 2004), although dynamics of mantle wedge melting and magma production in this geodynamic setting have not been yet quantified on the basis of numerical modelling, a deficit we address here. It is well-established that water plays a major role in generation of magmas within subduction zones (Stern, 2002). Generally water lowers the mantle solidus temperature (Takahashi and Kushiro, 1983), which ultimately drives melting of the mantle wedge material below magmatic arcs due to the flux of water originating from dehydration of the subducting slab (e.g., Davies and Stevenson, 1992; Ewart et al., 1998; Hasegawa et al., 1991; Kelley et al., 2006; Miller et al., 1994; Morris et al., 1990; Rose et al., 2001; Stern, 2002; Tatsumi, 1986). Thus, implementation of hydrous processes into a numerical code is vital for proper modelling of magma production dynamics during subduction. To account for these processes our model of active continental margins is based on a coupled petrological-thermomechanical approach (Gerya et al., 2006) that includes slab dehydration, water transport and melting processes. Through this model we aim to quantify wedge melting dynamics that cannot be obtained directly from nature and finally to obtain a basis for possible broad scale balancing of generated magma volumes.

In this paper we study magmatic productivity at convergent continental margins that are similar to fossil Pacific-type margins involving a pronounced accretionary wedge system in the fore-arc. We further compare our numerical results with critical natural observations available for this type of tectono-magmatic system.

2. Model setup

2.1. Initial configuration

We have developed a regional 2D model of an active margin including free slab bending, propagation of water released from the subducting slab and partial melting. The model spatial coordinate frame is 2500 km × 200 km and the initial geometry of the model (Fig. 1) corresponds to the onset of subduction at a passive continental margin (Regenauer-Lieb et al., 2001). In this model oceanic crust consists of (1) a relatively thin (1 km) heterogeneous layer of marine sediments, (2) a 2 km thick sequence of hydrothermally altered basalts (metabasalts), and (3) a 5 km section comprised largely of gabbroic rocks. A 1 km thick layer of serpentinized mantle is present at the base of the oceanic crust, as partial serpentinization of the oceanic slab mantle has been documented (Rupke et al., 2004). The continental crust consists of a 30 km thick layer of granodiorite. The subjacent mantle is considered to be anhydrous peridotite, whereas the overlying mantle is either anhydrous or hydrated ($\leq$2 wt% water) peridotite depending on the kinematic model for the propagation of slab fluids discussed below. Although mantle wedge rocks have the capacity to absorb up to 8 wt% water during serpentinization (Connolly, 2005), we adopt 2 wt% water as an upper limit to account for heterogeneous hydration resulting from channelization of slab-derived fluids (Davies, 1999) as consistent with observed mantle wedge seismic velocities (Carlson, 2001).

As consistent with the initiation of subduction by sedimentary loading at a passive margin (Regenauer-Lieb

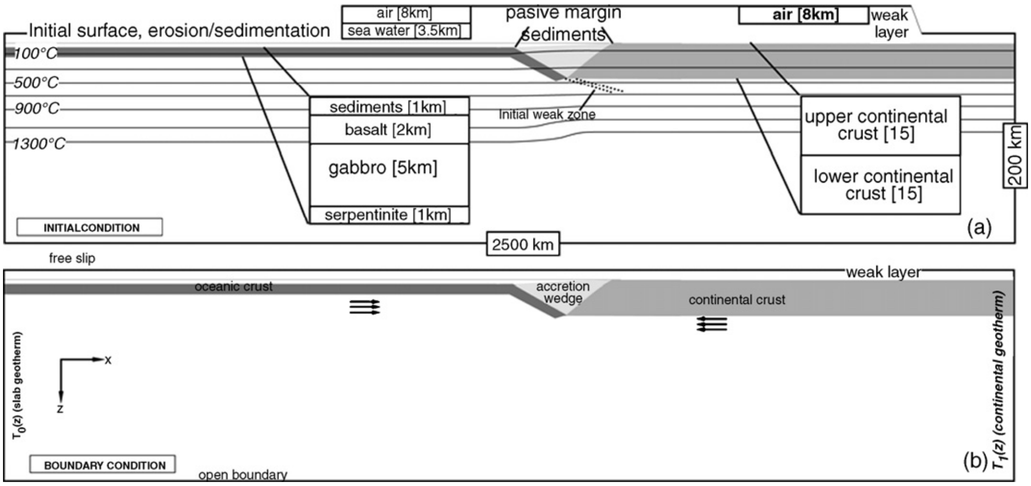

Fig. 1. Numerical model setup (see text for more details). Staggered grid resolution: 651 × 101 nodes, 10 million randomly distributed markers. Grid step vary from 2 km × 2 km in the subduction area to 10 km × 2 km outside of this area.

et al., 2001) we impose the site of subduction initiation below a sedimentary basin formed at the ocean-continent interface. The nucleated subduction zone is prescribed as a 4–10 km wide weak zone cutting across the entire mantle lithosphere and reaching depth of 60 km. The weak zone is prescribed as a wet brittle fault within mantle rocks, characterized by wet olivine rheological parameters and high pore fluid pressure. In combination, these factors permit initiation of the subduction process. During the subduction, the pre-defined weak zone is spontaneously replaced by weak subducted crustal rocks and hydrated (serpentinized) mantle formed in response to slab dehydration.

We have chosen initial conditions with a broad sedimentary wedge within the fore-arc of the continental margin. This allows for comparison of modelling results with the convergent continental margin of southern South America during late Paleozoic and Mesozoic times. Particularly, the dimensions chosen for the modelled specific fore-arc appear realistic when compared with the most recent situation in southernmost Chile: according to Bangs and Cande (1997) and Hervé et al. (2000) the width of the sediment fill in the recent trench basin in Southern Chile at 50°S amounts ~50 km, even wider further south. The current outcrop width of the Early Mesozoic accretionary prism in that region is similar. The whole fore-arc system of accreted sediments and present trench fill reaches a width of 150 km. Recent canyon/fan systems together with the actual trench basin fill reach a width of 150 km in south-central Chile at 40°S and the onshore current outcrop of the fossil arc system reaches further 100 km width (Glodny et al., 2005).

The initial temperature field in the oceanic plate is defined by an oceanic geotherm (Turcotte and Schubert, 2002) for a lithospheric age of 40 Myear. In the continental plate the initial thermal structure corresponds to a linear temperature profile limited by 0 °C at the surface and 1312, 1362 or 1412 °C (varied in different experiments, Table 1) at 100 km depth. The initial temperature gradient in the asthenospheric mantle below 100 km depth is 0.5 °C/km.

2.2. Boundary conditions

We implemented free slip conditions at all boundaries except for the lower one, which is permeable in both downward and upward directions. Infinite-like external free slip condition (Burg and Gerya, 2005) along the bottom imply free slip at 1200 km depth. Similarly to the usual free slip condition, external free slip allows global conservation of mass in the computational domain and is implemented by using the following limitation for velocity components at the lower boundary:

$$\frac{\partial v_x}{\partial z} = 0,$$
$$\frac{\partial v_z}{\partial z} = -\frac{v_z}{\Delta z_{\mathrm{external}}}$$

where $\Delta z_{\mathrm{external}}$ is the vertical distance from the lower boundary of the model to the external boundary where free slip ($\partial v_x/\partial z = 0,\ v_z = 0$) is satisfied (i.e. $\Delta z_{\mathrm{external}} = 1000$ km). In order to minimize mechanical interaction of the cold slab with the permeable lower boundary, the maximal viscosity at 20 km deep region along this boundary was limited to 10^{19} Pa s. Infinite-like external constant temperature conditions along the lower boundary are implemented by using the following limitation: $\partial T/\partial z = (T_{\mathrm{external}} - T)/\Delta z_{\mathrm{external}}$, where $T_{\mathrm{external}} = 1723$ °C at 1200 km depth at the external boundary.

The surface of the oceanic and continental crust is dynamically calculated as a free surface by using initially an 11–8 km-thick top layer with low viscosity (10^{18} Pa s) and density (1 kg/m^3 for the atmosphere, 1000 kg/m^3 for seawater prescribed in the weak layer below $z = 10$ km water level). The interface between this weak layer and the top of the oceanic crust deforms spontaneously and is treated as an erosion/sedimentation surface which evolves according to the transport equation (in Eulerian coordinates) solved at each time-step (Gerya and Yuen, 2003b).

$$\frac{\partial z_{\mathrm{es}}}{\partial t} = v_z - v_x\frac{\partial z_{\mathrm{es}}}{\partial x} - v_{\mathrm{s}} + v_{\mathrm{e}} \quad (1)$$

where z_{es} is a vertical position of the surface as a function of the horizontal distance x; v_z and v_x the vertical and horizontal components of material velocity vector at the surface; v_{s} and v_{e} are gross scale sedimentation and erosion rates, respectively, which correspond to the relation:

$$v_{\mathrm{s}} = 0, \quad v_{\mathrm{e}} = 0.3\ \mathrm{mm/year\ when}\ z < 9\ \mathrm{km},$$
$$v_{\mathrm{s}} = 0.03\ \mathrm{mm/year}, \quad v_{\mathrm{e}} = 0\ \mathrm{when}\ z > 10\ \mathrm{km}.$$

Erosion and sedimentation processes are implemented via a marker transmutation. The low viscosity of the weak top layer (10^{18} Pa s) creates a high viscosity contrast (>10^3) and causes minimal shear stresses (<10^4 Pa) along the erosion/sedimentation surface (Burg and Gerya, 2005). Test experiments have shown that choosing lower viscosities of the weak layer do not affect notably the development of the topography.

Plate motion is prescribed (Fig. 1b) by imposing locally constant velocities for the oceanic (at $x = 1000$ km) and the continental (at $x = 2000$ km) plates. Not prescribing the angle of subduction and velocity

Table 1
Description of numerical experiments

Run	Subduction rate, cm/yr	Overriding plate rate, cm/yr	Temperature at depth of 100 km (C°)	Plastic yield limit of sediments, MPa	Plastic yield limit of oceanic crust, MPa	Density mode[a]	$v_{z(\mathrm{percolation})}$, cm/yr[b]	$R_{\mathrm{H_2O}}$	Tectonic regime[c]
Model 1	2	0	1412	3	3	1	0.9	2.2	2
Model 2	2	0	1362	3	10	2	0.9	2.2	2
Model 3	2	0	1412	10	3	2	0.9	2.2	2
Model 4	2	1	1412	3	3	1	0.9	2.2	2
Model 5	2	2	1412	3	3	1	0.9	2.2	2
Model 6	2	3	1412	3	3	1	0.9	2.2	1
Model 7	2	0	1312	3	3	1	0.9	2.2	2
Model 8	2	0	1362	3	3	2	0.9	2.2	2
Model 9	2	0	1412	3	3	1	0.9	2.2	2
Model 10	4	0	1412	3	3	2	0.9	4.4	2
Model 11	4	0	1362	10	3	2	0.9	4.4	2
Model 12	4	0	1312	3	3	2	0.9	4.4	2
Model 13	4	0	1362	3	3	2	0.9	4.4	2
Model 14	4	0	1362	3	10	2	0.9	4.4	2
Model 15	4	0	1412	10	3	2	0.9	4.4	1
Model 16	4	0	1412	3	3	2	0.9	4.4	3
Model 17	4	1	1412	3	3	1	0.9	4.4	1
Model 18	4	3	1412	3	3	1	0.9	4.4	1
Model 19	4	3	1312	3	3	1	0.9	4.4	1
Model 20	6	0	1412	3	3	1	0.9	6.6	1
Model 21	6	0	1412	10	3	2	0.9	6.6	1
Model 22	6	0	1412	3	3	2	0.9	6.6	1
Model 23	6	1	1412	3	3	1	0.9	6.6	1
Model 24	6	2	1412	3	3	1	0.9	6.6	1
Model 25	6	3	1412	3	3	1	0.9	6.6	1
Model 26	8	0	1362	3	3	1	0.3	26.6	1
Model 27	2	0	1362	3	3	1	0.03	66.6	2
Model 28	2	0	1362	3	3	1	0.3	6.6	2
Model 29	2	0	1362	3	3	1	3	0.6	1
Model 30	6	0	1362	3	3	1	0.03	200	2
Model 31	6	0	1362	3	3	1	0.3	20	2
Model 32	6	0	1362	3	3	1	3	2	1

[a] 1 = simplified density model (Gerya and Yuen, 2003b); 2 = density is computed from the stable mineralogy for each lithology by free energy minimization approach (Connolly and Petrini, 2002; Gerya et al., 2006).

[b] $v_{z(\mathrm{percolation})}$ is the constant relative velocity of upward percolation of water through the mantle.

[c] 1, continuous plate coupling, compressional regime (Fig. 2); 2, trench retreat and opening of the back-arc basin, extensional regime (Fig. 3); 3 - hybrid regime: extension followed by compression (Fig. 5).

along the whole length of the slab allows for spontaneous slab bending below the trench area. In this case the dip angle of the subducting plate is mainly controlled by slab rheology and density as well as interaction with the surrounding mantle.

Principal details of the numerical modelling approach used in this paper are described in Appendix A.

3. Results

3.1. General development

At convergent margin settings hydrated oceanic crust is subducted into the upper mantle where dehydration processes take place and aqueous fluids are released from the slab. The loci for fluid and/or melt generation are determined by the intersection of dehydration reaction boundaries of primary hydrous minerals within the subducted lithosphere with slab geotherms. Due to dynamic release of water from the slab and mantle wedge hydration, Rayleigh–Taylor instabilities can develop above the subducting slab and trigger an upward migration of partially molten upwellings (Gerya and Yuen, 2003b). To investigate the chemical and volumetric development of these features we have performed 32 2D numerical experiments (Table 1). We tested the response of slab behaviour, melt generation and its evolution with time to changes of

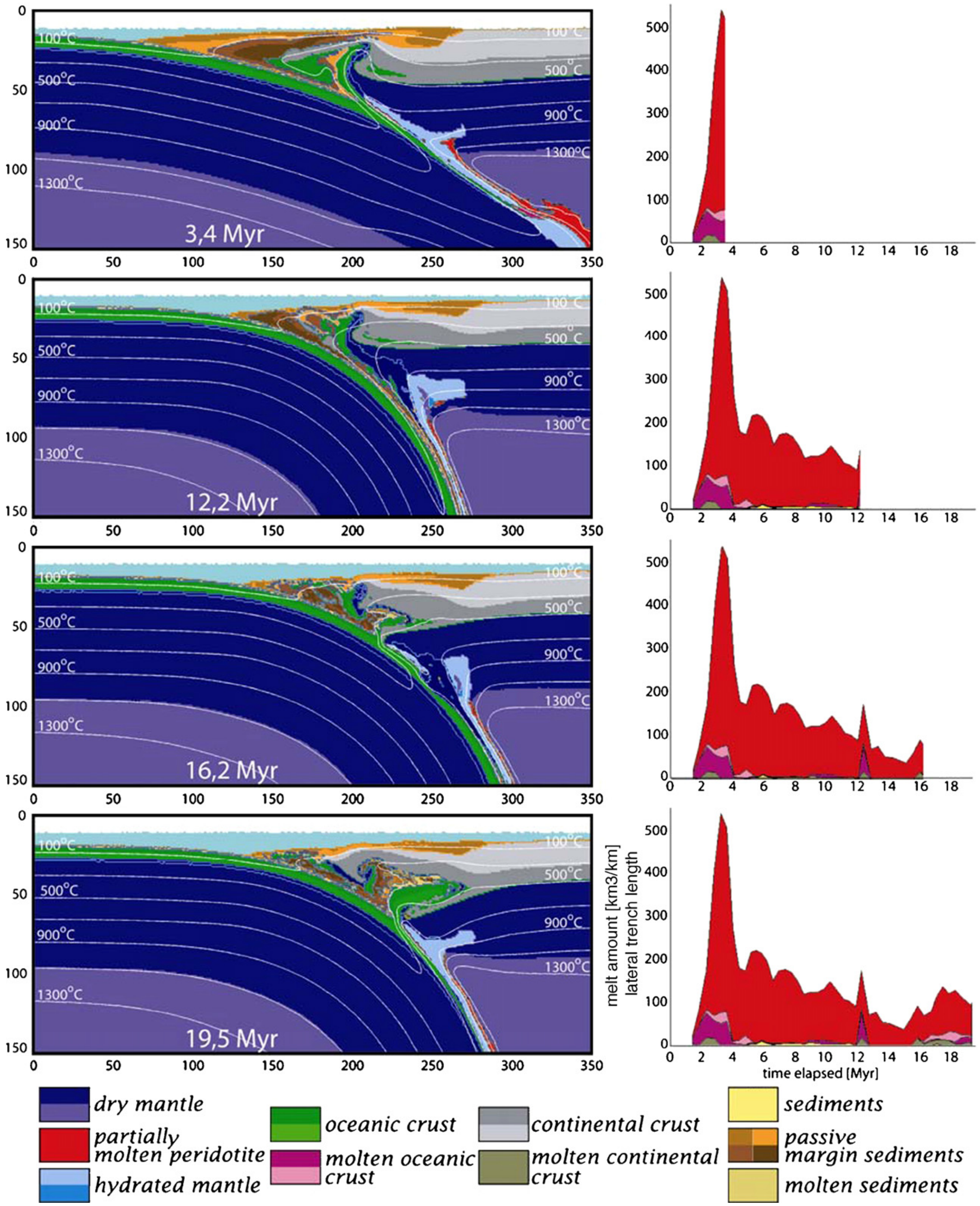

Fig. 2. Development of a stable convergence regime with continuous coupling of the plates (model 20, Tables 1 and 2). (Left) Evolution of the lithological field with time. (Right) Evolution of the amount of melt [km^3/km lateral trench length] in the mantle wedge as a function of time. Partially molten rocks stay deep in the mantle wedge below the lithosphere of the overriding plate. Further propagation of melts toward the surface can be related to the formation of magmatic channels (Gerya and Burg, 2007) that is not modelled here.

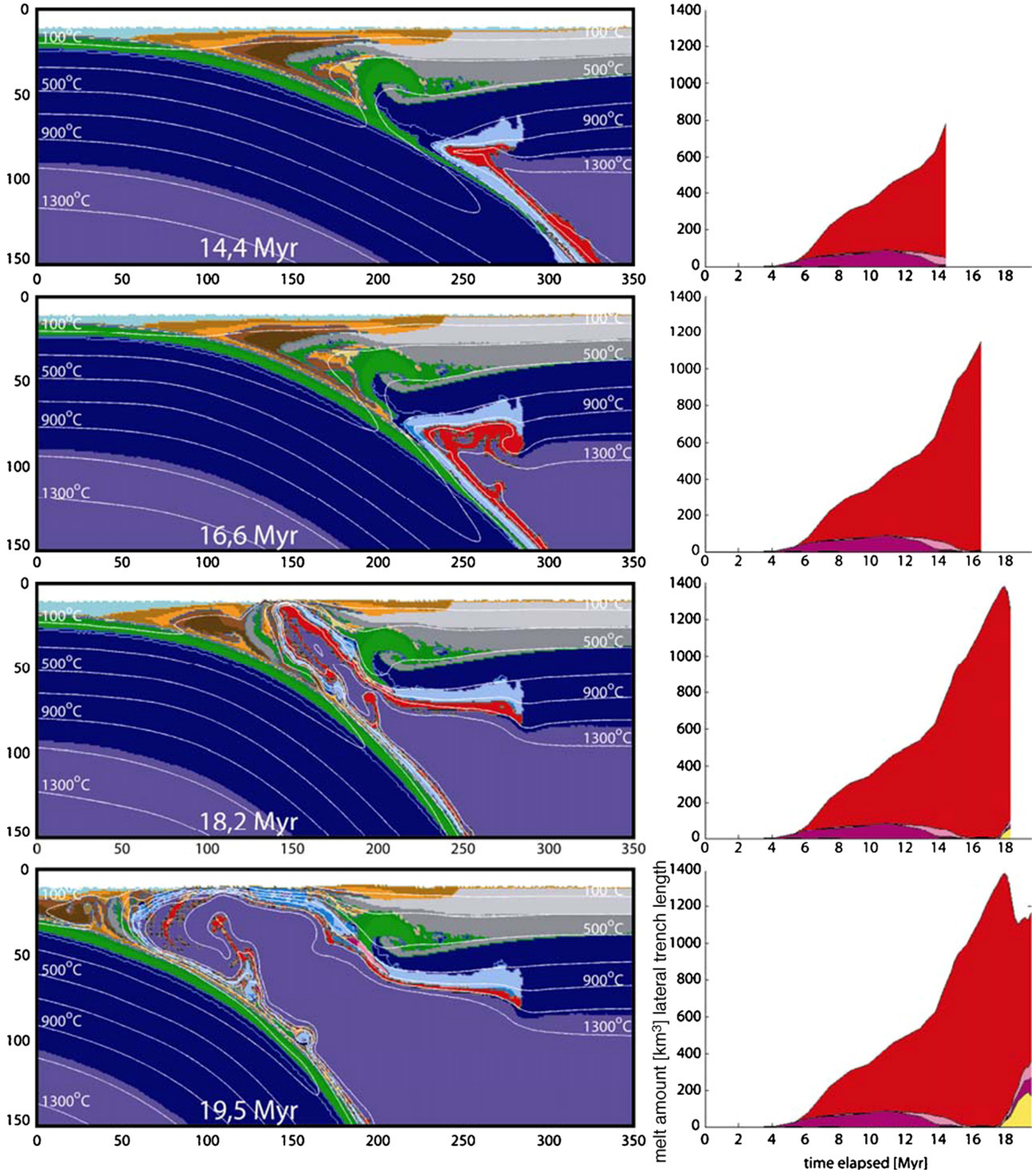

Fig. 3. Development of an extensional regime with slab retreat and decoupling of the plates (model 1, Tables 1 and 2). (Left) Evolution of the lithological field with time. (Right) Evolution of the amount of melt [km^3/km lateral trench length] in the mantle wedge as a function of time. Colour code as in Fig. 2.

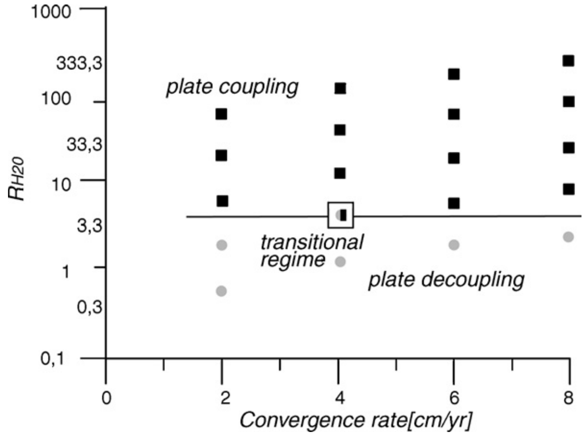

Fig. 4. Area diagram representing changes in the regime of subduction in the reference to dimensionless ratio R_{H_2O} (plate convergence rate divided by water propagation velocity) and convergence rate. Different symbols correspond to different regimes identified in numerical experiments (Tables 1 and 2): circles = extensional regime with plate decoupling, squares = stable convergence regime with plate coupling.

physical parameters controlling development of the model.

The investigated parameters are: the velocity of the subducting slab and the overriding plate, the velocity of upward percolation of water through the mantle, the strength of the oceanic crust and its sediments and also the initial temperature in the mantle wedge. With this approach we are able to determine which parameters play a dominant role in the development of some characteristic features observed in natural subduction systems.

3.2. Plate coupling and decoupling: two fundamental settings

Two fundamental regimes of subduction have been observed in our numerical experiments: (1) continuous coupling and convergence of the plates (Fig. 2) and (2) retreat of the slab, extension, and opening of a back-arc basin with a spreading centre in the middle (Fig. 3). Slab retreat is caused by uprise of hot, dry asthenospheric mantle along the weakened (hydrated) interface between the subducting slab and overriding plate (Fig. 3). Therefore, the intensity of this process is strongly dependent on growth dynamics of the hydrated weak zone above the slab which in turn depends on (i) water upward percolation velocity ($V_{z(\mathrm{percolation})}$, Appendix, Eq. (A7)) controlling widening of the hydration zone and (ii) plate convergence rate ($V_{(\mathrm{convergence})}$) controlling narrowing of this zone by simple shear deformation. Hence the major parameter controlling the development of the different two regimes of subduction (Fig. 4) is the dimensionless velocity ratio (R_{H_2O}).

$$R_{H_2O} = \frac{V_{(\mathrm{convergence})}}{V_{z(\mathrm{percolation})}}. \qquad (2)$$

The extensional regime is characteristic for relatively slow convergence rates ($R_{H_2O} < 4$). For faster convergence rates ($R_{H_2O} > 4$), the motion parameter is the dominating one and no other parameter seems to influence the slab behaviour (slab retreat appears with $R_{H_2O} \leq 3$ for all runs). In contrast, no slab retreat is observed in runs with $R_{H_2O} > 4$ (Fig. 5).

The bifurcation between the two dynamical regimes of subduction takes place around the velocity ratio of 4. At this transitional value of R_{H_2O} a hybrid regime of subduction can occur (Fig. 6): the initial extension and formation of the back-arc basin is followed by a compressional mode associated with shortening of the basin and subduction of the arc.

The influence of other model parameters on the coupling/decoupling phenomenon is less significant and only observed in experiments with transitional value of the velocity ratio $R_{H_2O} = 4$ (Table 1).

3.3. Variation of the slab angle with time and depth

In all experiments the slab bending radius and slab inclination vary with time. These variations correlate with the amount of convergence rather than with time. During the first 250–350 km of convergence after the beginning of subduction slab flattening occurs (Fig. 7). Then the slab radius decreases rapidly within 100–200 km of convergence, slab inclination becomes steeper and stabilizes. This strong oscillation of the slab angle is related to the initiation of subduction. The shallow episode is characteristic for the initial stage where the slab motion is solely governed by plate convergence, while further steepening of the plate is caused by growing influence of the slab pull. After that a weak slab unbending episode can be observed in most experiments and small fluctuations in slab dip develop (Fig. 7). The time and magnitude of the slab flattening event during this unbending episode is influenced by the physical parameters of subduction as follows:

(1) If the overriding plate is motionless, the increase in subduction rate leads to: (i) a steeper average slab dip angle (smaller slab bending radius) and (ii) a longer extent (wavelength) of the second unbending episode while the relative intensity (amplitude) of this episode followed by slab bending remains about the same (∼100 km, Fig. 7a). However, for a highest tested convergence rate of 8 cm/year the

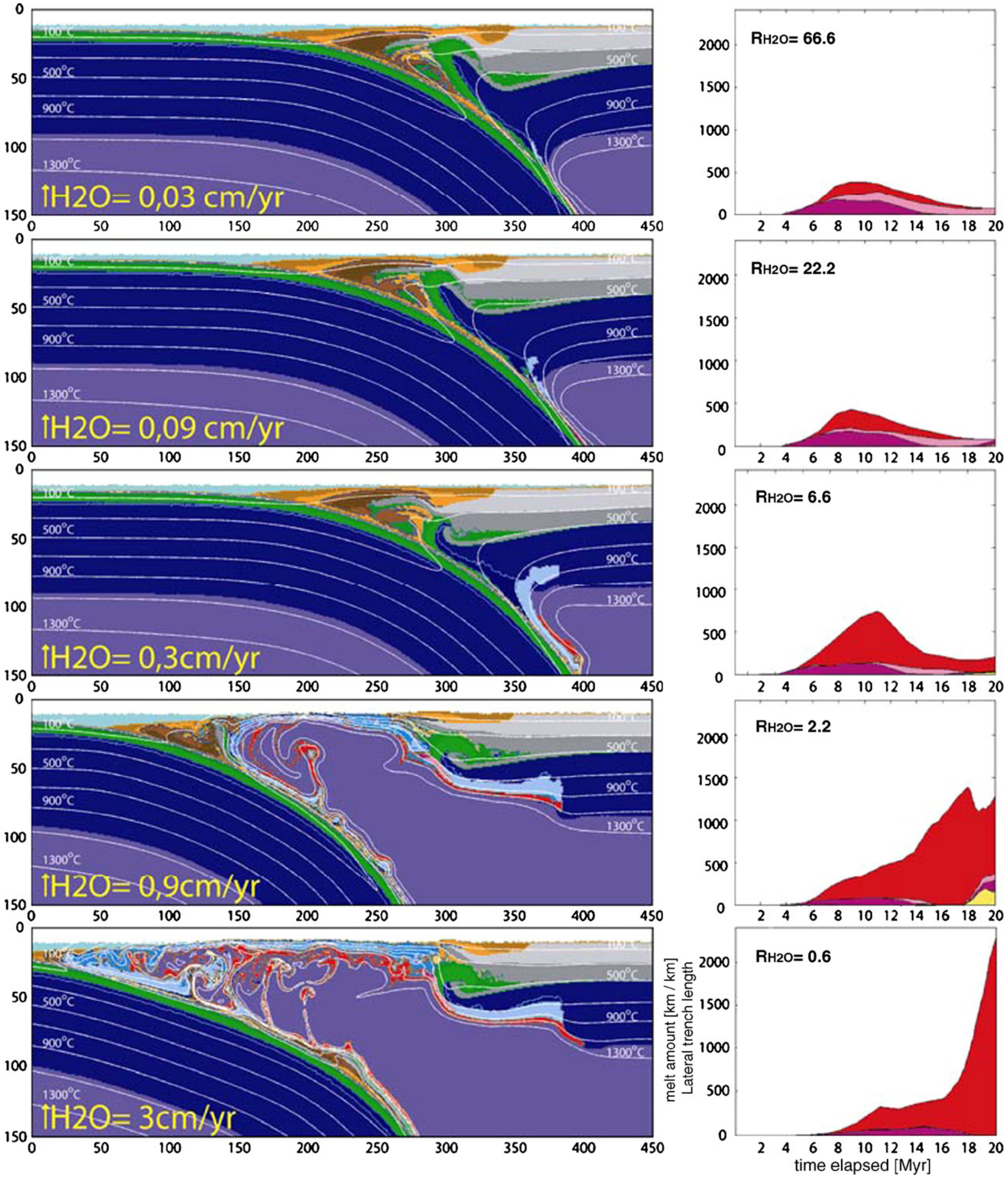

Fig. 5. (Left) 20 Myear time frames for experiments with different upward water propagation velocity for experiments with convergence rate of 2 cm/year. (Right) Evolution of the amount of melt [km^3/km lateral trench length] in the mantle wedge as a function of time respectively to the run represented on the left side. Colour code as in Fig. 2.

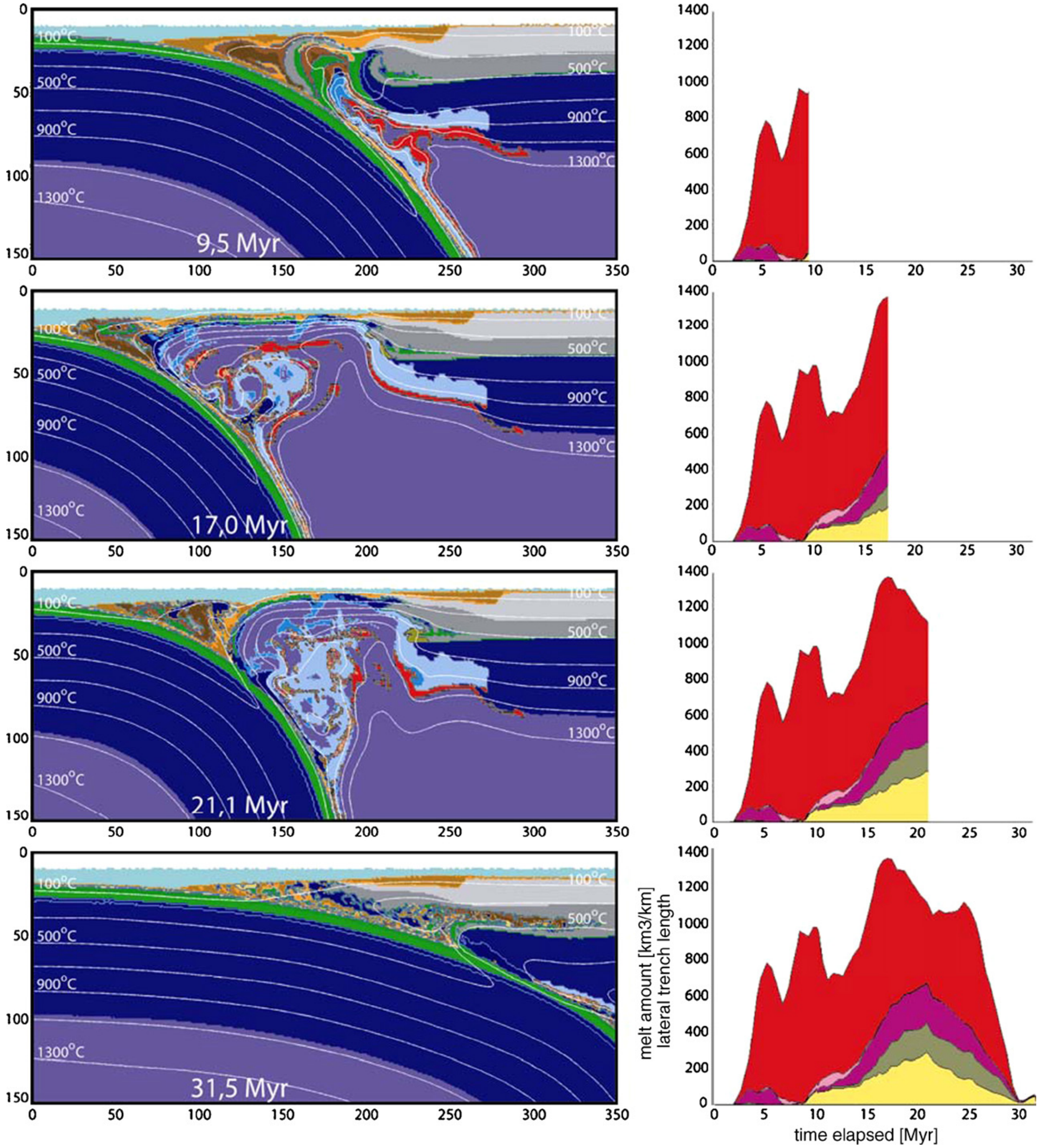

Fig. 6. Development of a hybrid subduction regime with slab retreat (decoupling of the plates) at the beginning of the run followed by change in the regime to compressional (model 16, Tables 1 and 2). (left) Evolution of the lithological field with time, (right) evolution of the amount of melt [km^3/km lateral trench length] in the mantle wedge as a function of time. Colour code as in Fig. 2.

unbending episode is not observed, the slab bending radius simply stabilises at a value of ∼200 km after ∼400 km of subduction. In contrast, in experiments with oceanward motion of the continent the increase of the slab radius during the second slab unbending episode is not followed by bending and the final slab curvature radius (480–500 km, Fig. 7b) is notably larger than in case of the immobile overriding plate

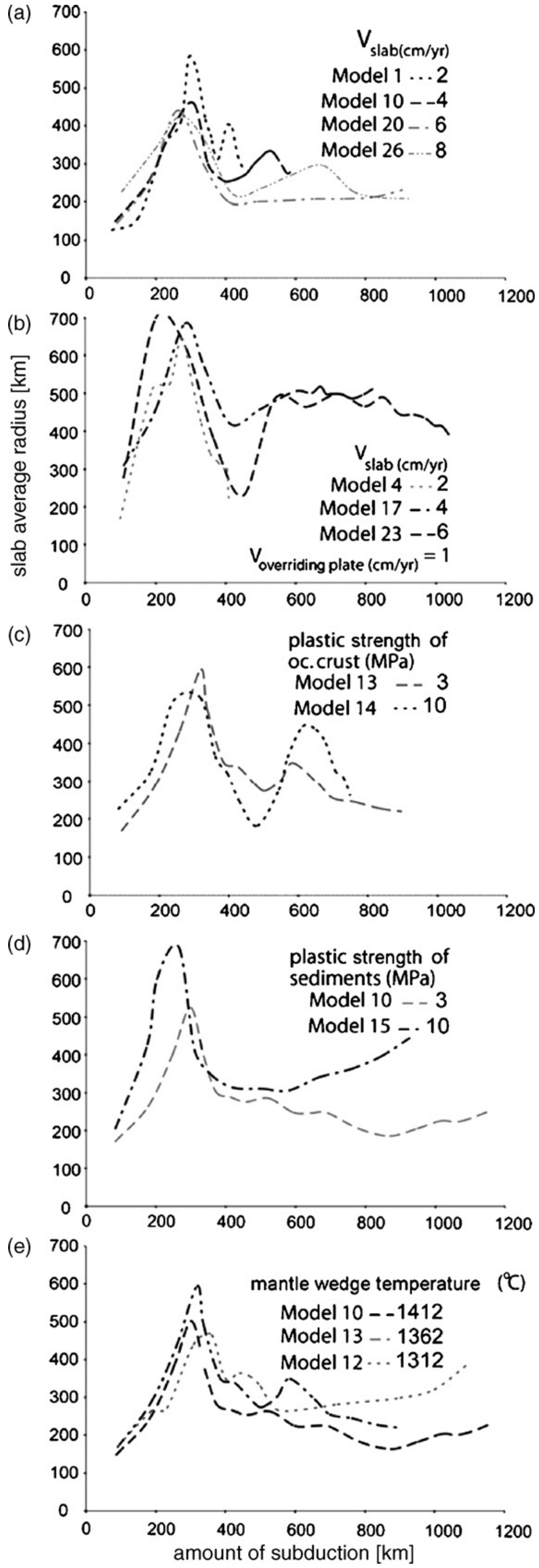

Fig. 7. Average slab curvature radius vs. amount of subduction with variation of following parameters: (a) variation in subduction rate with motionless continental plate, (b) variation in subduction rate with moving oceanward continental plate at rate of 1 cm/year, (c) plastic yield limit of oceanic crust, (d) plastic yield limit of sediments, (e) variation in the asthenospheric mantle temperature.

(200–300 km, Fig. 7a). This behaviour is consistent with previous studies (van Hunen et al., 2002) that report shallowing of the slab inclination angle with an increase of the velocity of the overriding plate.

(2) At a constant subduction rate an increase of the plastic yield limit of basaltic and gabbroic oceanic crust from 3 to 10 MPa causes an increase in the magnitude of slab curvature changes during the second unbending episode (Fig. 7c). In contrast, a similar increase of plastic strength of passive margin sediments located atop the oceanic crust increases the magnitude of the first slab unbending episode (Fig. 7d). In this case, a continuous decrease in the slab angle is also observed after 600 km of subduction.

(3) Variations in the asthenospheric wedge temperature do not influence the slab behaviour in a systematic way (Fig. 7e).

The magnitude of changes in the slab inclination angle increases with depth since deep parts of the slab are more easily bent than shallow parts (Fig. 8). In addition to the major unbending and bending episodes the slab angle tends to oscillate on a shorter subduction length scale of 20–50 km. These fluctuations are likely to occur due to variations in the average slab density caused by periodic formation and departure of positively buoyant partially molten thermal–chemical plumes from the slab (Figs. 2, 3, 5 and 6).

3.4. Dynamics of melt production

Our code is not designed to model magma segregation from solid residue as well as magma extraction processes. Therefore to quantify melt productivity dynamics, bulk amount of partially molten rocks (and not the amount of melt in these rocks) is calculated. This simplification allows us to avoid uncertainties in quantifying the actual amount of melt in partially molten rocks under high pressure conditions.

(1) At constant water percolation velocity molten rock production is dependent on the convergence rate: slow convergence rates favour

Table 2
Results of numerical experiments

Run	Average slab radius (km)	Maximum slab radius (km)	Time (Myear)	Amount of subduction (km)	Minimum slab radius (km)	Time (Myear)	Amount of subduction (km)	Average melt production (km^2/Myear)	Max melt production (km^2/Myear)	Time (Myear)	Amount of subduction (km)	Min melt production (km^2/Myear)	Time (Myear)	Amount of subduction (km)	Average melt amount in wedge (km^2)	Max melt amount in mantle wedge (km^2)	Time (Myear)	Amount of subduction (km)
Model 1	345.9	579.9	14.69	293.94	126	3.66	73.2	88.61	277	7.01	140.2	−177	18.25	365	1110.1	1662	22.68	453.6
Model 2	371.4	530.4	14.21	284.36	134	3.55	71	84	257	11.01	220.2	−220	17.27	345.4	985.6	1479	16.93	338.6
Model 3	836.87	1332	13.8	277.08	256.2	3.6478	72.95	44.4	251	10.76	215.2	−302	22.94	458.8	712.8	1172	16.82	336.4
Model 4	342.9	526.4	10.13	304.11	167.36	3.27	65.4	130.6	126	14.65	293	−1289	14.42	288.4	1439.9	2150	13.57	271.4
Model 5	337.2	521.3	7.80	312.12	132.4	2.98	119.2	20.2	243	4.5	180	−253	10.5	420	503	956	8.43	337.2
Model 6	326.8	532.48	6.59	329.92	147.68	2.4316	121.58	11.06	564	2.27	113.5	−236	9.14	457	476	886	7.65	382.5
Model 7	394.5	619	15.95	319	134	3.9	78	85	424	5.28	105.6	−187	19.8	396	1269.8	1785	19.8	396
Model 8	386.1	592.3	15.21	317	137.18	3.97	79.4	83.6	433	7.1	142	−129	18.56	371.2	1111.6	1507	27.95	559
Model 9	407.5	607.3	14.48	289.6	166.83	3.61	72.2	122	352	11.49	229.8	−136	18.91	378.2	1422.6	2215	21.5	430
Model 10	292.8	459.7	7.68	307.54	148.71	2.07	41.4	47.432	423	3.24	64.8	−278	6.05	121	1069.7	1762	15.85	317
Model 11	264.2	361	6.16	246.6	167.36	2.27	90.8	4	567	2.03	81.2	−205	4.34	173.6	409.1	825	12.43	497.2
Model 12	336.7	465.5	8.99	359.98	170	2.26	45.2	91.47	672	2.97	59.4	−250	18.64	372.8	906.2	1339	12.83	256.6
Model 13	319.5	593.8	7.96	318.65	167.57	2.25	45	123.7	504	2.02	40.4	−217	14.44	288.8	1265.3	1916	23.84	476.8
Model 14	751.38	1118	7.97	318.9	225.39	2.0317	81.26	34.4	443	1.81	72.4	−139	5.8	232	599	908	14.17	566.8
Model 15	630.2	1138	6.78	271.2	318.47	2.33	93.21	13.38	622	2.08	83.2	−322	10.46	418.4	462.57	905	8.84	353.6
Model 16	303.1	524.7	7.46	298.52	170.7	2.77	55.4	2.9	583	1.84	36.8	−517	26.58	531.6	686.2	1346	17.09	341.8
Model 17	656.2	1783	5.65	282.49	309	2.17	108.5	7.22	578	1.96	98	−153	3.89	194.5	330.7	630	6.67	333.5
Model 18	278.2	468	4.0519	243.1	186.2	1.87	112.2	4.86	409	1.69	101.4	−211	2.95	177	218	534	3.98	238.8
Model 19	296.5	452.5	5.0552	353.86	185.7	2.1891	153.2	4.46	422	1.97	137.9	−69	3.43	240.1	328.6	547	3.43	240.1
Model 20	235.8	440	4.35	261.35	143.5	1.46	87.6	5.7	505	1.47	88.2	−314	3.02	181.2	149.3	528	3.02	181.2
Model 21	529	1194	4.24	254.4	289.6	1.47	88.2	0.73	461	1.32	79.2	−283	2.92	175.2	91.5	469	2.92	175.2
Model 22	267.8	444.3	5.33	319.86	184.3	1.46	87.6	10.84	560	1.47	88.2	−258	8.62	517.2	430.7	827	7.23	433.8
Model 23	565.3	1420	4.09	286.38	276.1	1.55	108.53	−0.5556	419	1.39	97.3	−265	2.76	193.2	132.1	468	2.76	193.2
Model 24	525	1523	3.44	275.4	315.3	1.27	102	5.3	435	1.19	95.4	−375	2.1	168.4	142.4	454	2.51	201.3
Model 25	489.1	1487	3.69	295.4	333.5	1.27	114.3	7.5	467	1.01	91.3	−342	2.13	192.4	104.2	438	2.215	199.4
Model 26	556.34	1555	3.37	269.6	325.12	1.27	101.62	8.2	460	1.15	92	−356	2.36	188.8	113.4	495	2.36	188.8

Computed average, maximal and minimal values for slab radius and melt production.

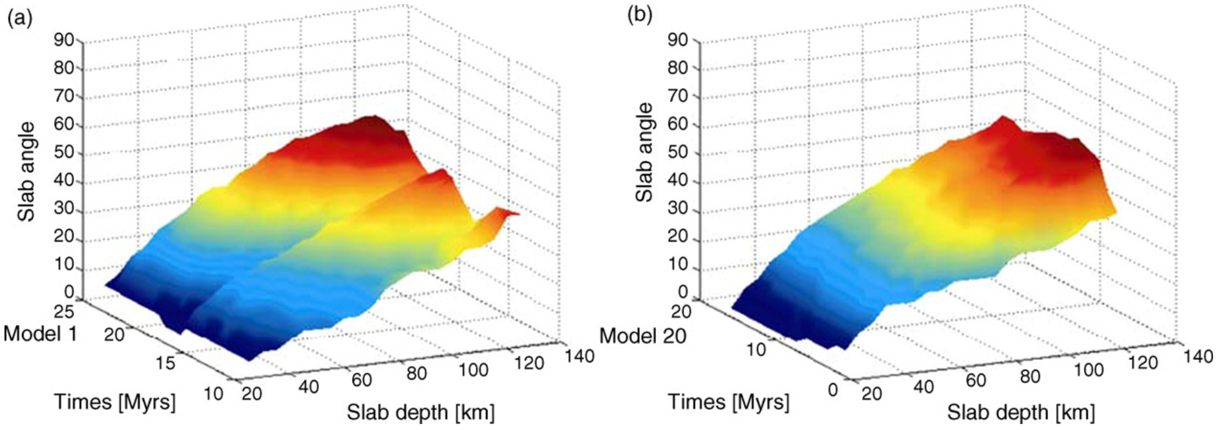

Fig. 8. Computed slab angle as a function of time and depth, (a) Model 1 in Tables 1 and 2 corresponds to Fig. 3, (b) Model 20 (Tables 1 and 2) corresponds to Fig. 2. See text for discussion.

melting (Figs. 9 and 10, Table 2). The following tendency is quantified in experiments with immobile overriding plate: the average melt productivity for 2 cm/year convergence rate is 88.61 km^2/Myear, for 4 cm/year the amount of melt halves (47.43 km^2/Myear), and for 6 and 8 cm/year it decreases by one order of magnitude (8.2 km^2/Myear and 5.7 km^2/Myear, respectively). This trend also occurs for the advancing (1 cm/year, Fig. 10) overriding plate: 0.56 km^2/Myear for a convergence rate of 7 cm/year, 7.22 km^2/Myear for 5 cm/year, and 130.6 km^2/Myear for 3 cm/year.

(2) An increase in the asthenospheric mantle temperature increases the amount of partially molten crustal rocks in the wedge (Fig. 11). This effect is caused by more intense generation of mixed (subducted crust + hydrated mantle) plumes rising from the slab (Gerya et al., 2006; Gorczyk et al., 2006).

(3) The increase in the plastic strength of the oceanic crust causes an increase of melting of crustal components, but it lowers the degree of partial melting in the mantle wedge (Fig. 12). This phenomenon occurs mainly due to an increase in the strength of the subduction channel melange and decrease in the volume of subducted melange rocks which are the major source of water for asthenospheric wedge hydration and melting. An increase in the plastic strength of sediments significantly decreases both the amount of crustal and mantle melting (Fig. 13), since strong sediment layer atop the slab suppresses delamination. Consequently, water is released into the colder overriding lithosphere rather than into the hot mantle wedge.

3.5. *Contrasting evolution of melt productivity with time in different settings*

The overall evolution of melt productivity shows contrasting behaviour for the two different regimes of subduction:

(1) In runs with continuous plate coupling, i.e. a compressive setting (Fig. 2), the highest amount of melt appears at an early stage and decreases with time. This decrease is caused by quenching of molten materials induced by increasing pressure during their descent together with the subducted slab. Generation of partially molten plumes is also restricted in this regime.

(2) Experimental runs in which plate decoupling appears, i.e. extensional settings (Fig. 3), show high melt productivity that increases with the opening of a back-arc basin. The same tendency is shown for slab melts that become dominant during later stages of subduction (after 16–19 Myear). The increased melt production triggers a mantle plume. This plume causes necking of the lithosphere and the necking triggers the retreat of the slab. Thus the amount of back-arc spreading controls the slab retreat.

In both settings considerable amounts of partially molten rocks are lost from the model through the lower boundary being dragged down by the subducting slab. Due to a rapid increase of the solidus temperature with increasing pressure such partially molten rocks would be quenched at depth. This quenching effect must be taken into account in any attempt to balance melt production in a specific regional segment of a convergent margin.

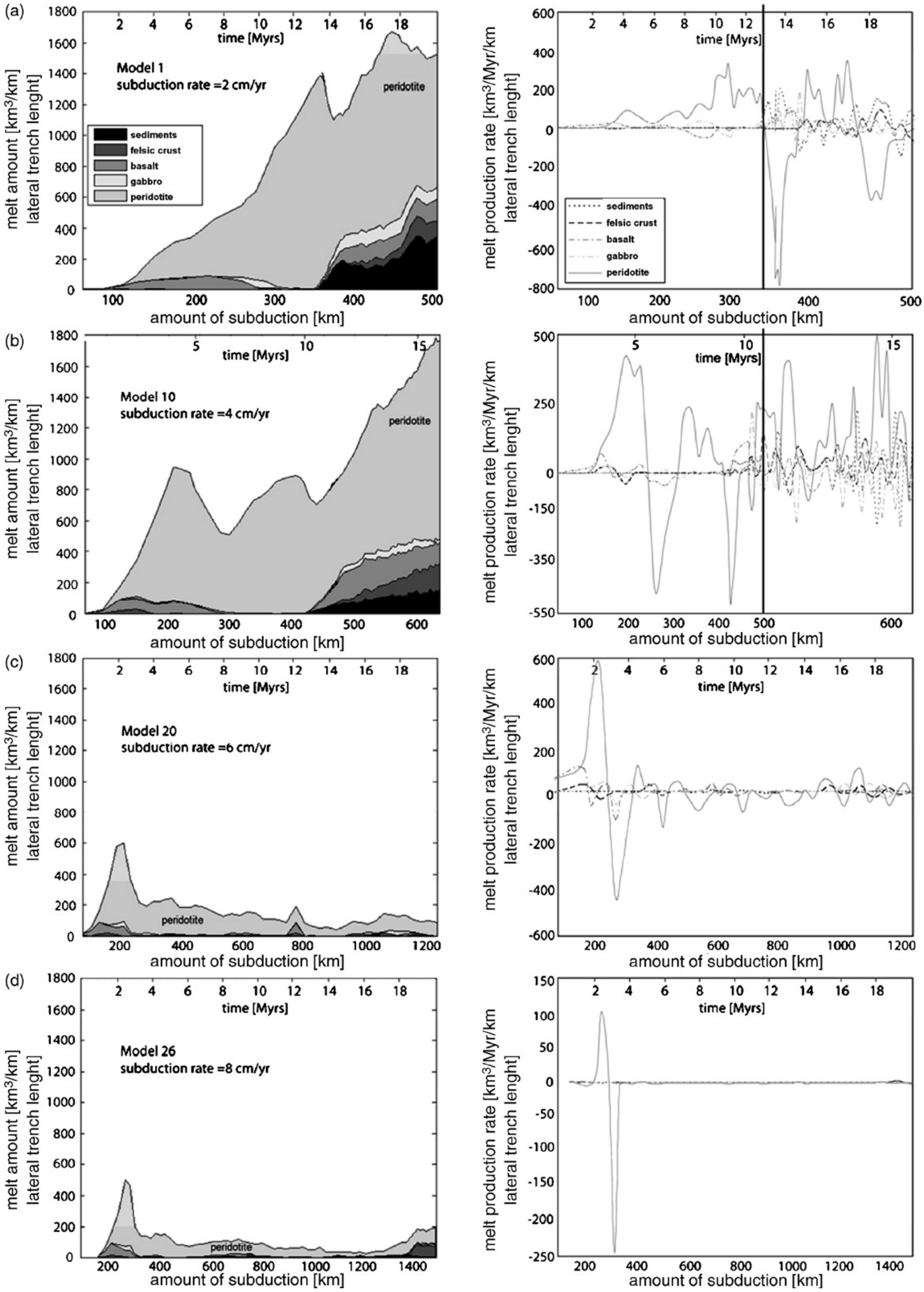

Fig. 9. Amount of molten rocks occurring in the mantle wedge (left column) and rate of production of these rocks (right column) as a function of the amount of subduction and time elapsed, for runs with various subduction rates and motionless overriding plate. (a) Model 1 (Tables 1 and 2) corresponds to Figs. 3 and 7a; (b) Model 10; (c) Model 20 corresponds to Figs. 2 and 7a; (d) Model 26 corresponding to Fig. 7a. Thick horizontal line in right diagrams indicates change of the scale.

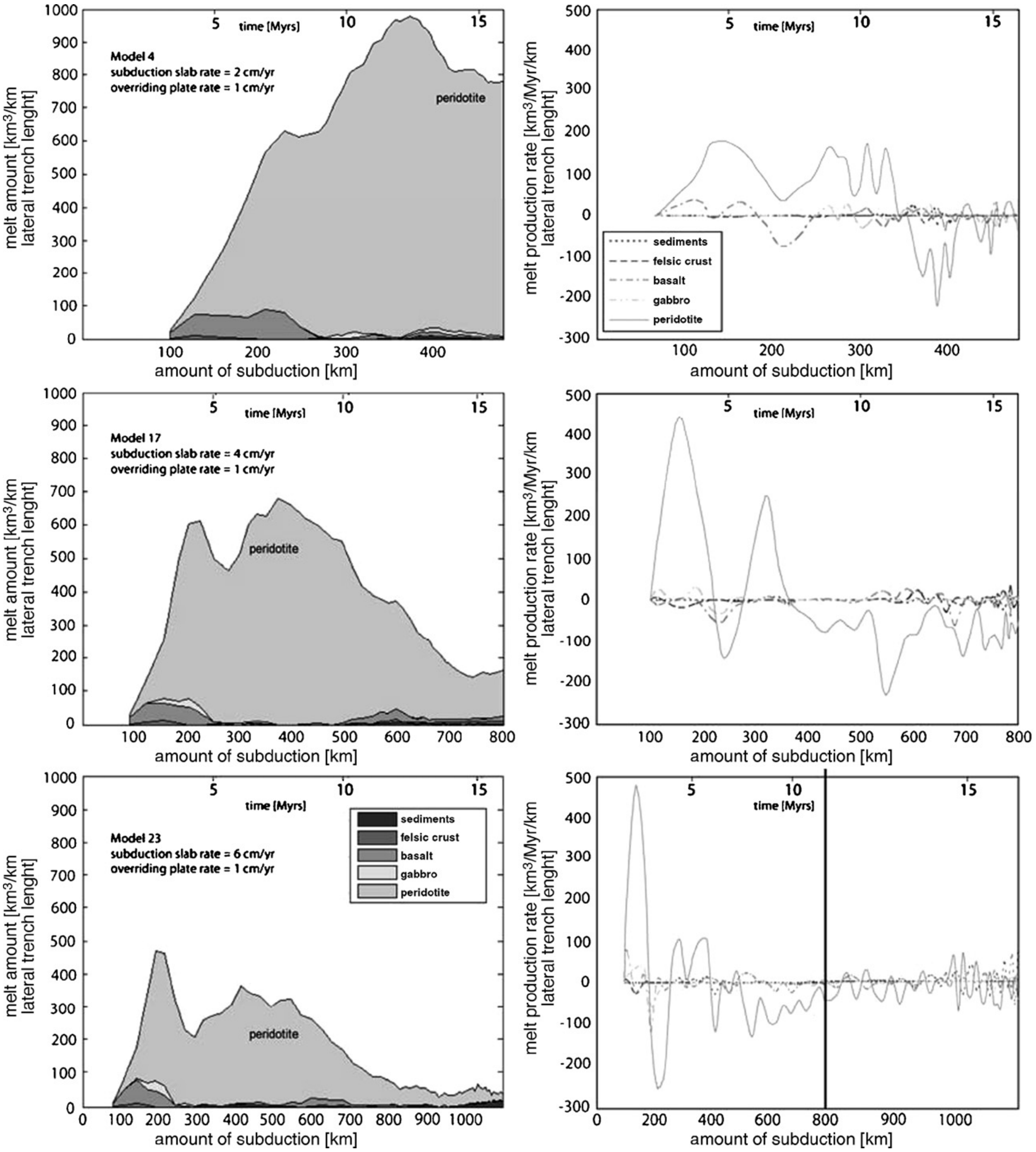

Fig. 10. Amount of molten rocks occurring in the mantle wedge (left column) and rate of production of these rocks (right column) as a function of the amount of subduction, for runs with various convergence rate. (a) Model 4 (Tables 1 and 2), corresponding to Fig. 7b; (b) Model 17; (c) Model 23.

(3) In case of a transitional subduction regime characterized by a change from extensional to compressional tectonics (Fig. 6) an increase in melt productivity is observed during the opening of the back-arc basin. This opening and related asthenospheric rise is slower then in the previous case and is not associated with the formation of a distinct spreading center. Consequently, the melt productivity growth is com-

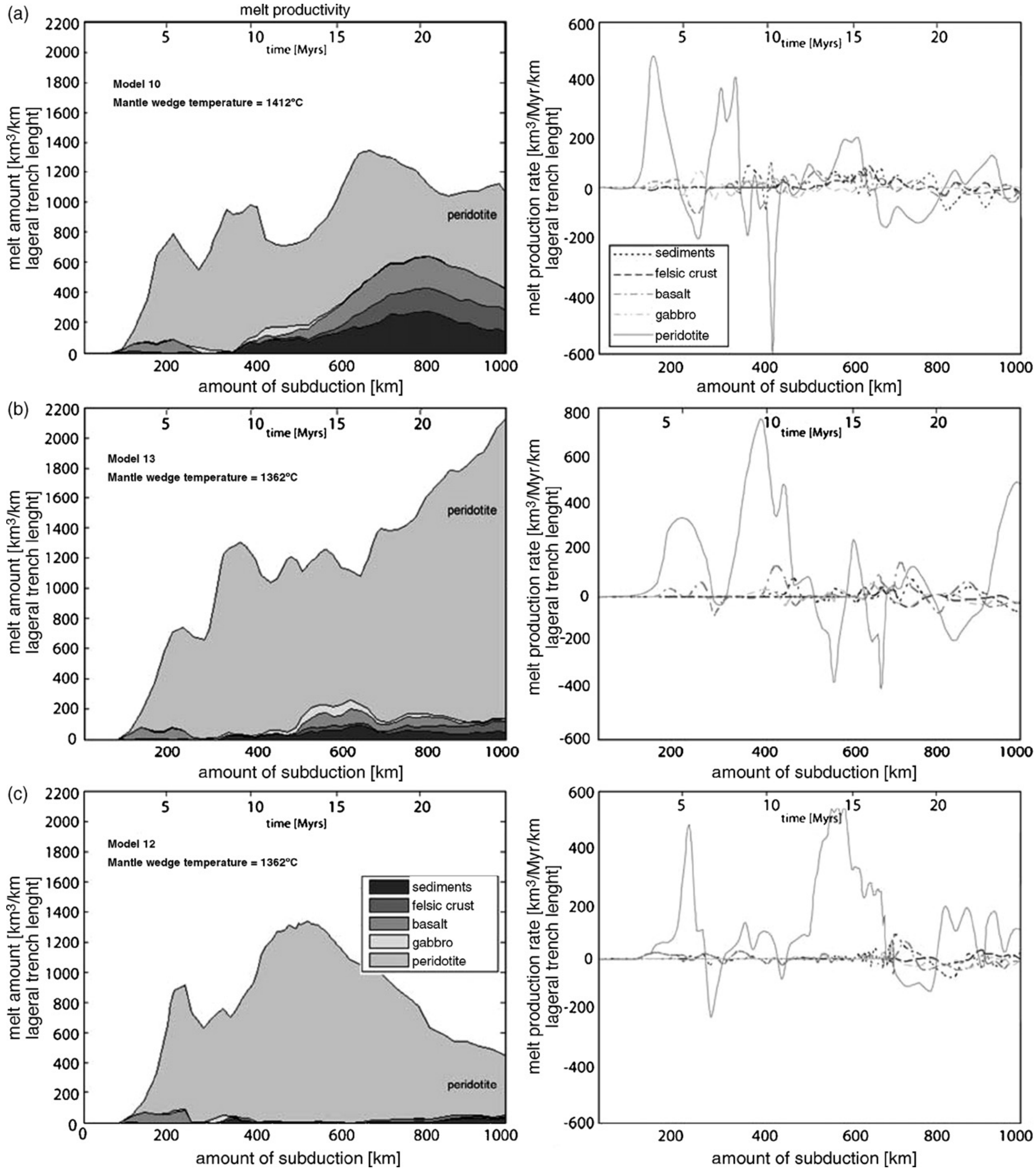

Fig. 11. Amount of molten rocks occurring in the mantle wedge (left column) and rate of production of these rocks (right column) as a function of the amount of subduction and time elapsed, for runs with various athenospheric mantle temperature; initial mantle wedge temperature at 100 km varies: (a) 1412 °C for Model 10 (Tables 1 and 2) corresponding to Fig. 7e; (b) 1362 °C for Model 13; (c) 1312 °C for Model 12.

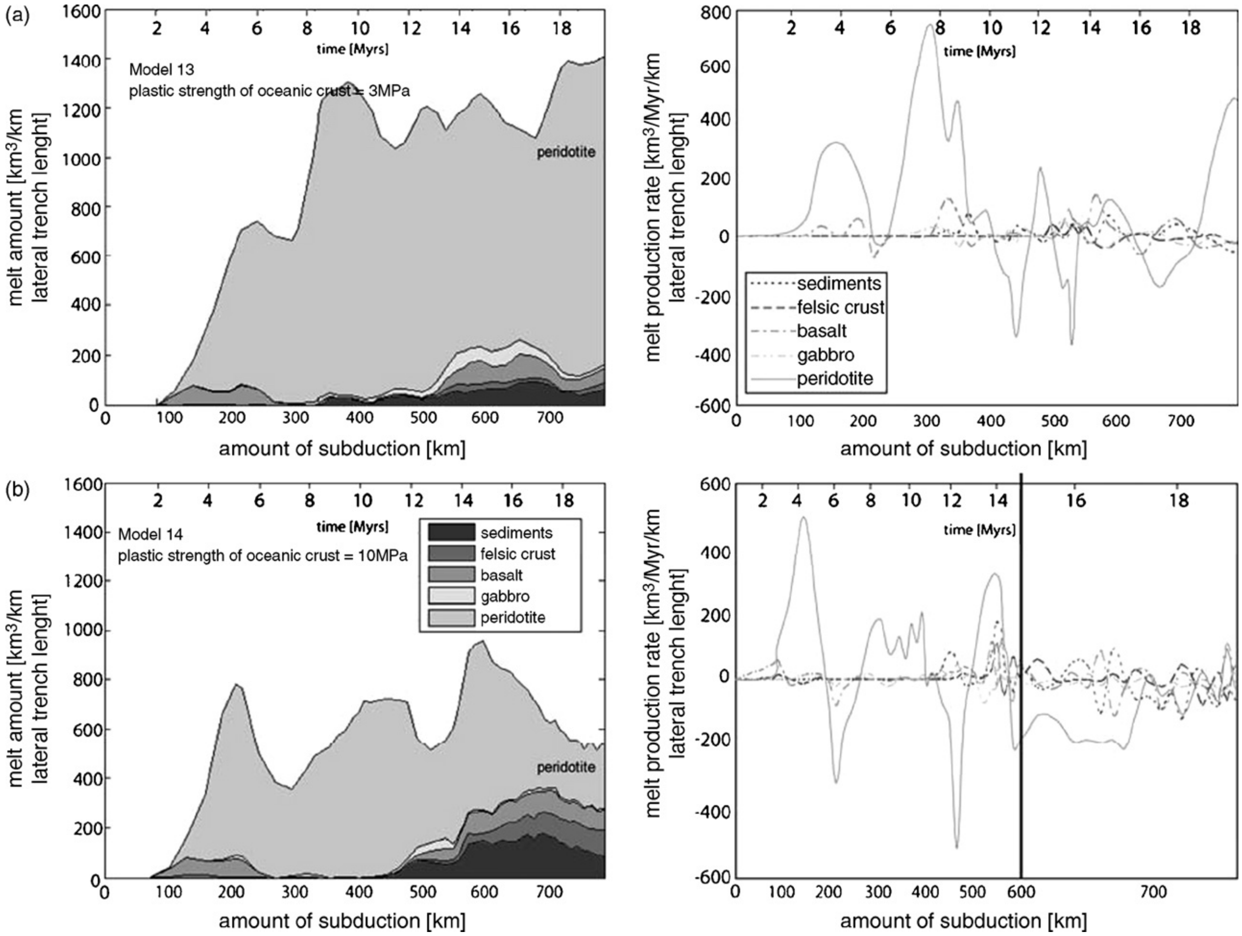

Fig. 12. Amount of molten rocks occurring in the mantle wedge (left column) and rate of production of these rocks (right column) as a function of the amount of subduction, for runs with various oceanic crust strength (a) Model 13 (Tables 3 and 4) corresponding to Fig. 7c; (b) Model 14.

plicated by fluctuations (cf. Figs. 3–6) caused by competing contributions of (i) decompression melting due to rise of material and (ii) subsequent cooling and quenching of molten rocks close to the surface.

4. Comparison with particular time-restricted evolutions at the South American convergent margin in central and southern Chile

Along the western margin of South America a convergent margin involving formation of pronounced accretionary prism systems only occurred during late Paleozoic times in central Chile and during Mesozoic times in southern Chile, when climatic conditions caused a high flux of detritus. The end of accretion and concomitant processes in the magmatic arc were controlled by considerable changes of the slab geometry between compressive and extensional regimes (Hervé et al., 2000; Willner et al., 2005). Hence two contrasting situations evolved that may directly be compared with our two distinct sets of numerical experiments.

(1) Compressive convergent conditions with the development of a broad accretionary prism and a concomitant magmatic arc prevailed during Late Paleozoic times in central Chile (section A in Fig. 14) and lasted for about 100 Myear (from ∼320 to ∼220 Ma (Willner et al., 2005)). The accretionary prism underwent a mass flow cycle involving subduction, underplating, ductile thinning, exhumation, erosion and resedimentation. Shortly after the beginning of this process the magmatic arc contemporaneously evolved at ∼300 Ma with a volumetrically dominant intrusive pulse, and the amount of melts steadily decreased afterwards (Hervé et al., 1988; Willner et al., 2005). This resembles the similar tendency in the experimental run shown in Fig. 2. The main magma intrusion pulse is

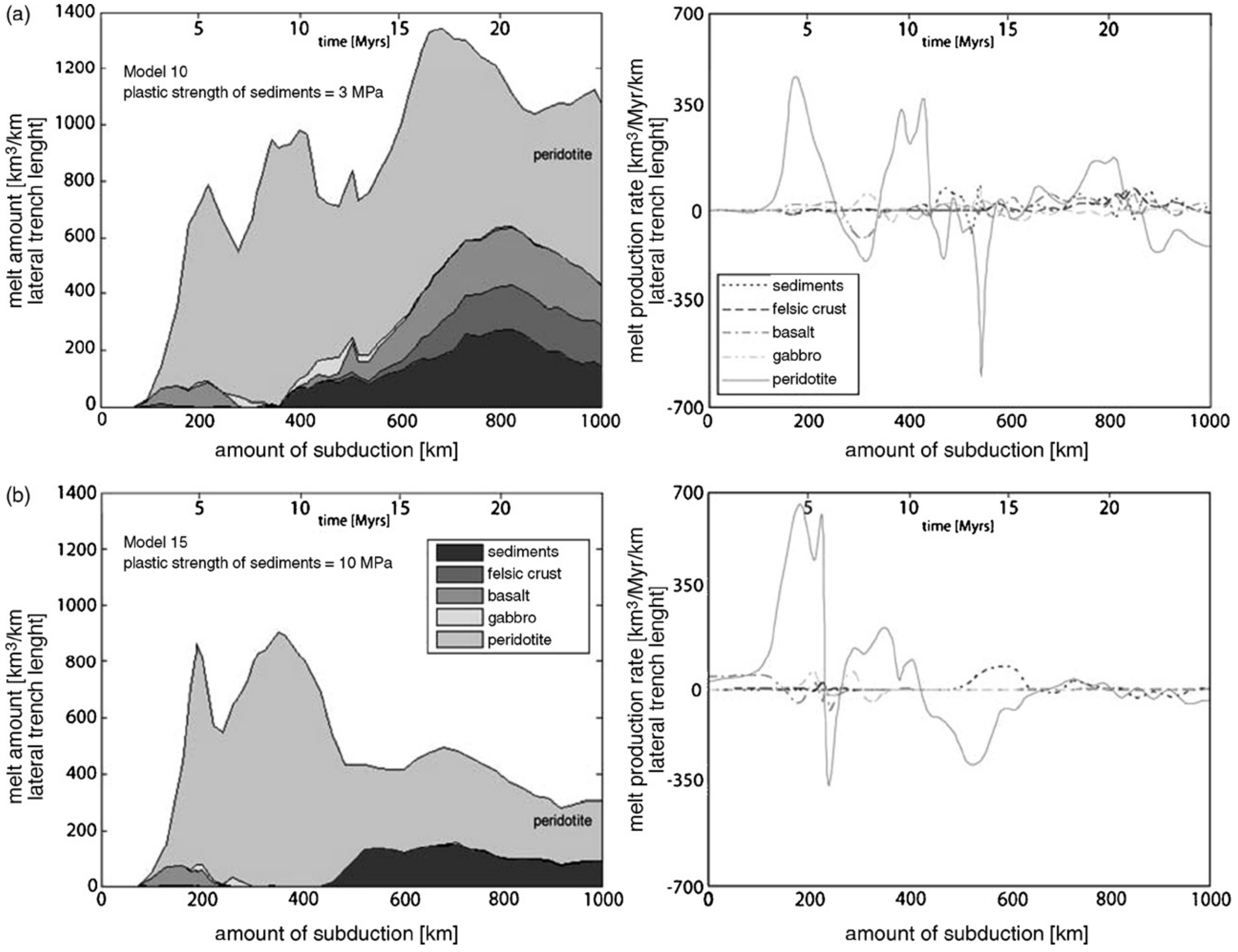

Fig. 13. Amount of molten rocks occurring in the mantle wedge (left column) and rate of production of these rocks (right column) as a function of the amount of subduction, for runs with various sediment strength (a) Model 16 (Tables 1 and 2), corresponding to Fig. 7d; (b) Model 15.

accompanied by widespread high temperature/low pressure metamorphism at ∼300 Ma. The melts of this late Paleozoic magmatic arc contain a high percentage of recycled crustal components (up to 80%) in spite of the fact that the crust was only slightly thickened (Lucassen et al., 2004). This might be explained by strong local heat advection and local rise of the initial temperature gradient due to mantle upwelling at the boundary between the accretionary prism and the continent at an early stage, a particular feature that may also be observed in the experiment shown in Fig. 2 and that caused local necking of the lithosphere. In the numerical experiment no new fertile mantle can be hydrated in the mantle wedge at an evolved stage and the rise of magma towards the surface is limited. Both effects cause waning intrusion with time in compressive settings with continuous plate coupling. Exhumation rates of the late Paleozoic accretionary prism in central Chile are in the order of 0.2–0.6 mm/year, in the magmatic arc 0.03–0.05 mm/year (Glodny et al., 2005; Willner et al., 2005). Both rates are consistent with erosion as the dominant mechanism for exhumation but are two orders of magnitude lower than the usual subduction rates. Furthermore steepening of the slab angle should have occurred 20 Myear after start of the evolution of this convergent margin at ∼320 Ma: intrusion of the arc magmas at 300 Ma occurred into an already formed upper level of the accretionary prism. Later the slab angle must have flattened again during continuous convergence until 220 Ma allowing only small and waning amounts of calcalkaline magma to rise. Hence short-time oscillation of the dip of the subduction slab is the primary cause of magma production in this setting.

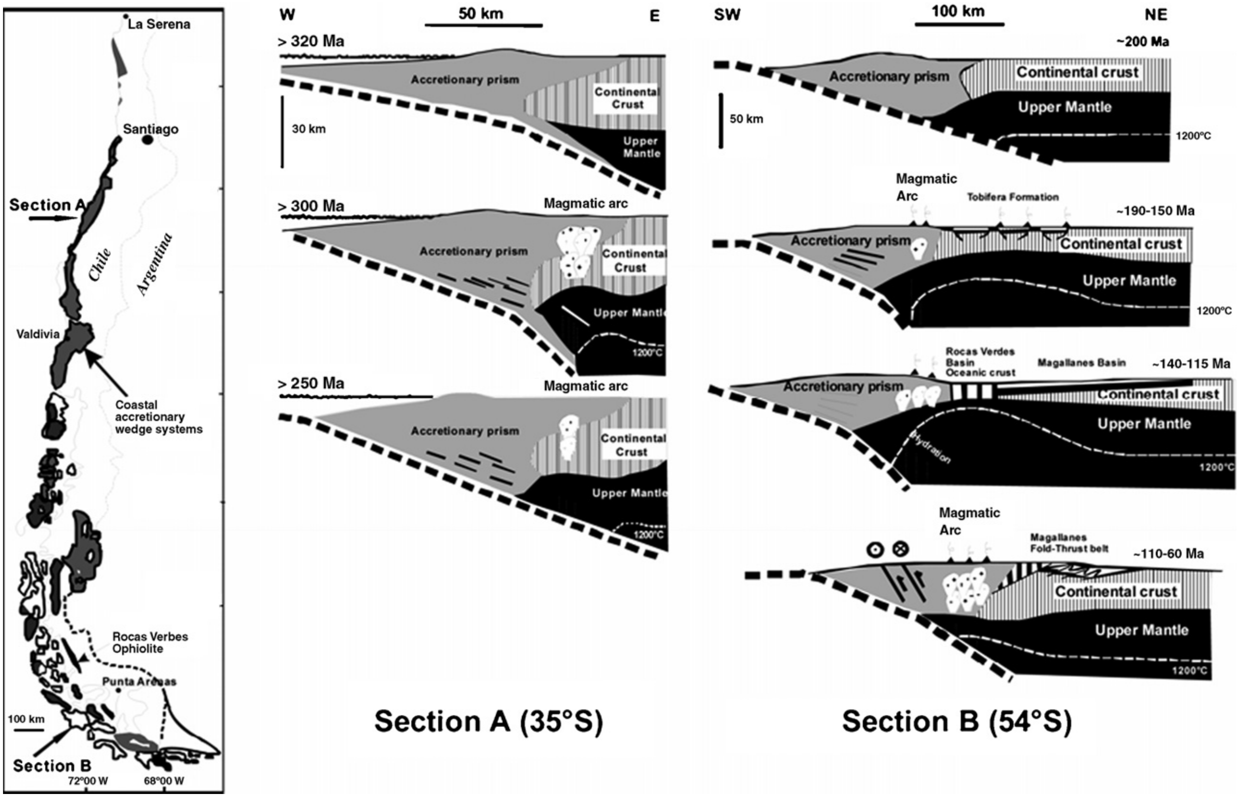

Fig. 14. Scenarios of two contrasting evolutions of active margins in Chile simulated by experimental runs in Figs. 2 and 3, respectively: Section A at 35°S represents the evolution of a convergent margin during Late Paleozoic times in central Chile, Section B at 54°S an extensional marginal setting during Mesozoic times in southermost Chile including opening of a back-arc basin.

(2) During late Triassic times (∼220 Ma) convergence conditions changed, accretion ceased and during slab retreat extensional Triassic basins opened in central Chile (Willner et al., 2005). Exhumation rates dropped by an order of magnitude to 0.04–0.06 mm/year and hence the convergence rate must have slowed. This change in slab geometry was presumably accompanied by a change of climatic conditions to a less humid climate causing a reduced sediment flux into the trench basin. The extensional setting during Triassic times was accompanied by production of extensive volumes of rhyolite and granite as well as minor basalt in central and southern Chile (Choiyoi magmatic province; Ramos and Kay, 1991).

Whereas in central Chile a coherent thinned continental margin was maintained during Mesozoic times, a wide oceanic back-arc basin developed in southern Chile during Cretaceous times as a consequence of extreme extension similar to the modelled slab retreat in Fig. 3: The Fuegan Andes of southernmost Chile (south of 50°S; section B in Fig. 14) constitute the only part along the South American margin where the retreat of the subducting slab led to back-arc spreading and formation of oceanic crust as observed in the South Patagonian Rocas Verdes basin during earliest Cretaceous times around ∼141–137 Ma (Hervé et al., 2000; Wilson, 1991). Prior to this event a wide early Mesozoic accretionary prism developed along the southernmost Chilean margin (234–195 Ma; Thomson and Hervé, 2002) and pronounced rifting resulted in bimodal magmatism (widespread rhyolite covers of the Jurassic Tobifera Formation at 190–150 Ma and intrusion of the Darwin Granite Suite at ∼164 Ma (Hervé et al., 2000). Opening of this back-arc ocean occurred in the western part of the Magallanes foreland basin, when the earlier formed early Mesozoic accretionary system in the fore-arc was separated from the continent (Hervé et al., 2000; Wilson, 1991). At Diego de Almagro Island accretion was still going on at ∼117 Ma and a gabbroic suite occurred as early arc intrusions in the Fuegan Batholith at 141–103 Ma. Pronounced intrusion of calcalkaline magmas of the Fuegan Batholith (Beagle Canal Plutonic

Group) occurred later at ∼113–81 Ma as synkinematic magmatism during renewed convergence and closure of the Rocas Verde and Magallanes basins (Hervé et al., 2000; Wilson, 1991). Post-tectonic activity in the magmatic arc followed at 60–34 Ma with intrusion of tonalite and monzodiorite of the South Seno Ano Nuevo Plutonic Group. The late intrusion of the dominant portion of calcalkaline melt during evolution of this extensional margin matches our experiment in Fig. 3. The contrasting magma evolution compared to that in central Chile is caused by the possibility of a steady rise of magma towards the surface and a steady rise of fertile mantle that becomes hydrated and partially molten. Comparable to the natural example we also observed closure of the back-arc basin in one experimental run about 5 Myear after opening involving flattening of the slab (Fig. 6). In this experiment shortening mainly occurs in the fore-arc area and also slight subduction erosion of continental crust and partly recycling in the accretionary system can be observed. Although main shortening in the natural example occurred in the foreland according to Wilson (1991), Willner et al. (2004) show that in a major convergent shear zone that attached the accretionary system to the continent again subducted continental crust was incorporated. This is a rare phenomenon in the convergent margin of Chile and was interpreted as direct evidence for the process of subduction erosion.

5. Conclusions

In this paper we study magmatic productivity at convergent continental margins that are similar to fossil Pacific-type margins involving a pronounced accretionary wedge system constituting the fore-arc. Such situations are time dependent due to the necessity for climatic conditions that allow large sediment fluxes into the trench basin.

Our numerical experiments show strong correlation between the magmatic productivity and tectonic regime that is strongly dependent on the dimensionless ratio (R_{H_2O}) between convergence rate and upward water percolation velocity. This ratio regulates growth dynamics of the hydrated weak zone above the slab resulting in either rheological coupling or decoupling between the plates. The compressional regime associated with a continuous plate coupling and relatively low melt production is characteristic for higher convergence rates ($R_{H_2O} > 4$). On the contrary, an extensional regime associated with plate decoupling, trench retreat, back-arc spreading and high melt productivity associates with relatively slow convergence rates ($R_{H_2O} < 4$). Results of our petrological–thermomechanical modelling involving water transport and melting, thus, strongly complement previous simplified studies of slab retreat, where authors investigated effects of density (e.g., Chase, 1978; e.g., Uyeda and Kanamori, 1979), viscosity (Enns et al., 2005) and lateral width (Schellart et al., 2007) of the slab.

At long-lived convergent margins such as at the Pacific coast of South America, frequent changes of compressive and extensional settings occur, that influence magma production in the arc. The comparison of our experiments with natural examples fits predicted and observed geodynamic behaviour of the tectonic systems, i.e. fossil situations at the margins in central and southern Chile, where pronounced accretionary systems developed in Late Paleozoic and Mesozoic times followed by periods of slab retreat and extension. Because these studied processes are particularly important precursors of continental collision, natural examples should be taken from a continental margin that was not involved in a continental collision during its evolution.

Acknowledgements

This work was supported by ETH Research Grants TH-12/04-1, TH-12/05-3, SNF Research Grant 200021-113672/1, by the RF President Program “Leading Scientific School of Russia” (grant #HLLI-5338.2006.5 to T.V.G.) and the RFBR grant #06-05-64098 (to T.V.G.) and by grant MA1160/24-1 by Deutsche Forschungsgemeinschaft to A.P.W. We greatly appreciate constructive reviews and very valuable suggestions of two anonymous reviewers.

Appendix A. Numerical method

A.1. Governing equations

The momentum, continuity, and thermal equations for the two-dimensional creeping-flow, accounting for thermal and chemical buoyancy, are solved using the modified I2VIS code (Gerya and Yuen, 2003a) based on conservative finite differences and a nondiffusive-marker-in-cell technique. The conservation of mass is approximated by the incompressible continuity equation:

$$\frac{\partial v_x}{\partial x} + \frac{\partial v_z}{\partial z} = 0 \qquad \text{(A1)}$$

The 2D Stokes equations take the form:

$$\frac{\partial \sigma_{xx}}{\partial x} + \frac{\partial \sigma_{xz}}{\partial z} = \frac{\partial P}{\partial x} \qquad \text{(A2)}$$

Table A1
Material properties used in 2D numerical experiments

Material	Thermal conductivity (W/(mK))	Rheology	Temperature of wet solidus (K)
Sedimentary rocks, continental crust	$0.64+\frac{807}{T+77}$	Wet quartzite flow law, $c=3$–10 MPa, $\sin(\varphi)=0$	$889+17{,}900/(P+54)+20{,}200/(P+54)^2$ at $P<1200$ MPa, $831+0.06P$at $P>1200$ MPa
Upper oceanic crust (altered basalt)	$1.18+\frac{474}{T+77}$	Wet quartzite flow law, $c=3$–10 MPa, $\sin(\varphi)=0$	$973{,}370{,}400/(P+354)+77{,}800{,}000/(P354)^2$ at $P<1600$ MPa, $935+0.0035P+0.0000062P^2$ at $P>1600$ MPa
Lower oceanic crust (gabbro)	-//-	Plagioclase (AN_{75}) flow law, $c=3$ MPa, $\sin(\varphi)=0.15$	-//-
Serpentinized mantle	$0.73+\frac{1293}{T+77}$	Constant viscosity Wet olivine flow law, $c=3$ MPa, $\sin(\varphi)=0$	–
Hydrated unserpentenize d mantle[a]	-//-	Wet olivine flow law, $c=3$ MPa, $\sin(\varphi)=0$	$1240+49{,}800/(P+323)$ at $P<2400$ MPa, $126630.0118P+0.0000035P^2$ at $P>2400$ MPa
Dry mantle	-//-	Dry olivine flow law, $c=1$ MPa, $\sin(\varphi)=0.6$	–
Continental crust	$0.64+\frac{807}{T+77}$	Wet quartzite flow law, $c=3$ MPa, $\sin(\varphi)=0.15$	$889+17{,}900/(P+54)+20200/(P+54)^2$ at $P<1200$ MPa, $831+0.06P$at $P>1200$ MPa
References	References	Gerya et al. (2002), Ranalli (1995)	Poli and Schmidt (2002), Schmidt and Poli (1998)

[a] Hydrated mantle beyond the serpentine stability field (Schmidt and Poli, 1998), $T>751+0.18P-0.000031P^2$ at $P<2100$ MPa, $T>1013-0.0018P-0.0000039P^2$ at $P>2100$ MPa.

$$\frac{\partial\sigma_{zz}}{\partial z}+\frac{\partial\sigma_{xz}}{\partial x}=\frac{\partial P}{\partial z}-g\rho(T,P,C,M) \tag{A3}$$

The density $\rho(T,P,C,M)$ depends explicitly on the temperature (T), the pressure (P), the composition (C), and the mineralogy (M).

The thermal equation is formulated as (Gerya and Yuen, 2003b):

$$\rho C_p\left(\frac{\mathrm{D}T}{\mathrm{D}t}\right)=-\frac{\partial q_x}{\partial x}-\frac{\partial q_z}{\partial z}+H_\mathrm{r}+H_\mathrm{a}+H_\mathrm{S}+H_\mathrm{L},$$

$$q_x=-k(T,C)\frac{\partial T}{\partial x},\ q_z=-k(T,C)\frac{\partial T}{\partial z},\ H_\mathrm{a}=T\alpha\frac{\mathrm{D}P}{\mathrm{D}t},$$

$$H_\mathrm{S}=\sigma_{xx}\dot{\varepsilon}_{xx}+\sigma_{zz}\dot{\varepsilon}_{zz}+2\sigma_{xz}\dot{\varepsilon}_{xz} \tag{A4}$$

where D/Dt is the substantive time derivative; x and z denote, respectively, the horizontal and vertical coordinates; σ_{xx}, σ_{xz}, σ_{zz} the components of the deviatoric stress tensor; $\dot{\varepsilon}_{xx}$, $\dot{\varepsilon}_{xz}$, $\dot{\varepsilon}_{zz}$ the components of the strain rate tensor; P the pressure; T the temperature; q_x and q_z the heat fluxes; ρ the density; g the gravitational acceleration; $k(T,C)$ the thermal conductivity, a function of composition and temperature (Table A1), e.g., Thompson and Hovis (1979); C_p the isobaric heat capacity; H_r, H_a, H_S, and H_L denote, the radioactive, adiabatic, shear and latent heat production, respectively.

A.2. Rheological model

The effective creep viscosities of solid rocks are represented as a function of temperature and stress by experimentally determined flow laws (Table A1). Viscosity for dislocation creep depending on strain rate, pressure and temperature is defined in terms of deformation invariants (Ranalli, 1995) as:

$$\eta_\mathrm{creep}-(\dot{\varepsilon}_\mathrm{II})^{(1-n)/2n}F(A_\mathrm{D})^{-1/n}\exp\left(\frac{E+VP}{nRT}\right) \tag{A5}$$

where $\dot{\varepsilon}_\mathrm{II}=1/2\,\dot{\varepsilon}_{ij}\dot{\varepsilon}_{ij}$ is the second invariant of the strain rate tensor and A_D, E, V and n are experimentally determined flow law parameters, respectively material constant, activation energy, activation volume and stress exponent. F is a dimensionless coefficient depending on the type of experiments on which the flow law is based. For example:

$$F=\frac{2^{(1-n)/n}}{3^{(1+n)/2n}},\quad \text{for triaxial compression and}$$

$$F=2^{(1-2n)/n},\quad \text{for simple shear.}$$

The ductile rheology of solid rocks is combined with a brittle rheology to yield an effective visco-plastic rheology. For this purpose the Mohr–Coulomb yield criterion

Table A2
Phases and thermodynamic data sources

Phase	Formula	Source
Antigorite	$Mg_{48x}Fe_{48(1-x)}Si_{34}O_{85}(OH)_{62}$	Rupke et al. (2004)
Clinoamphibole	$Ca_{2-2w}Na_{z+2w}Mg_{(3+2y+z)x}Fe_{(3+2y+z)(\tilde{1}x)}Al_{3-y-w}Si_{\underset{.}{7}+w\underset{.}{+}y}O_{22}(OH)_2,\ w+y+z \le 1$	Wei and Powell (2003), White et al. (2003)
Biotite	$KMg_{(3-w)x}Fe_{(3-w)(1-x)}Al_{1+2w}Si_{3-w}O_{10}(OH)_2,\ x+y \le 1$	Holland and Powell (1998)
Chlorite	$Mg_{(5-y+z)x}Fe_{(5-y+z)(1-x)}Al_{2(1+y-z)}Si_{3-y+z}O_{10}(OH)_8$	Holland et al. (1998)
Coesite	SiO_2	
Clinopyroxene	$Na_{\tilde{1}y}Ca_yMg_{xy}Fe_{(1-x)y}Al_ySi_2O_6$	Holland and Powell (1996)
Fluid	H_2O	Connolly and Trommsdorff (1991)
Garnet	$Fe_{3x}Ca_{3y}Mg_{3(1-x-y)}Al_2Si_3O_{12}$, $x+y \le 1$	Holland and Powell (1998)
Kyanite	Al_2SiO_5	
Lawsonite	$CaAl_2Si_2O_7(OH)_2 \cdot (H_2O)$	
Mica	$K_xNa_{\tilde{1}x}Mg_yFe_zAl_{3-2(y+z)}Si_{3+y+z}O_{10}(OH)_2$	Holland and Powell (1998)
Melt	Na–Mg–Al–Si–K–Ca–Fe hydrous silicate melt	Ghiorso et al. (2002)
Olivine	$Mg_{2x}Fe_{2(1-x)}SiO_4$	Holland and Powell (1998)
Orthopyroxene	$Mg_{x(2-y)}Fe_{(1-x)(2-y)}Al_{2y}Si_{2-y}O_6$	Holland and Powell (1996)
Plagioclase	$Na_xCa_{\tilde{1}x}Al_{\tilde{2}x}Si_{2+x}O_8$	Newton et al. (1980)
Sanidine	$Na_xK_{1-x}AlSi_3O_8$	Thompson and Hovis (1979)
Stishovite	SiO_2	
Talc	$Mg_{(3-y)x}Fe_{(3-y)(1-x)}Al_{2y}Si_{\tilde{4}y}O_{10}(OH)_2$	Holland and Powell (1998)

Unless indicated otherwise thermodynamic data was taken from Holland and Powell (1998). The compositional variables w, x, y, and z may vary between zero and unity and are determined as a function of pressure and temperature by free-energy minimization. Thermodynamic data for the iron endmember for antigorite solution was estimated as described in reference Rupke et al. (2004).

(Ranalli, 1995) is implemented by limiting creep viscosity, η_{creep}, as follows:

$$\eta_{\text{creep}} \le \frac{c + P\sin(\varphi)}{(4\dot{\varepsilon}_{\text{II}})^{1/2}}, \tag{A6}$$

where c is the cohesion (residual strength at $P = 0$) and φ is effective internal friction angle (Table A1).

All partially molten rocks are assigned to a reduced effective viscosity of 10^{17} Pa s (Pinkerton and Stevenson, 1992) which provides large viscosity contrast with the surrounding dry mantle (10^{19}–10^{26} Pa s).

A.3. Mineral composition and melt content

The stable *mineralogy* for each lithology with except of the continental crust is obtained by free energy minimization (Connolly and Petrini, 2002) as a function of pressure and temperature from thermodynamic data (Table A2). For this purpose, phase relations were resolved on a grid with a resolution of 5 K and 25 MPa. Examples of phase diagrams computed for different lithologies (Table A3) are discussed by Connolly and Kerrick (2002); Kerrick and Connolly (2002). The range of physical and chemical conditions considered here requires extrapolation of the silicate melt model (Ghiorso et al., 2002). Therefore, to ensure consistency with experimentally constrained melting boundaries employed in our earlier work (Gerya and Yuen, 2003b), calculations were done for each lithology with and without the silicate melt model. Physical properties are computed from these results depending upon whether melt is predicted to be stable from the experimentally constrained phase relations (Table A1). To account for thermal and density effects of phase transformations for the model development we employ the incompressible fluid approximation for the continuity equation and numerical smoothing of thermal and density effects due to phase changes for the momentum and temperature equation (Gerya et al., 2006; Willner et al., 2004).

A.4. Water migration

At the onset of subduction the lithologies water contents indicated in Table A2 are assigned to the oceanic crust including a lower serpentinite layer, and the surrounding mantle is anhydrous. To simulate the migration of water released by dehydration reactions, if water is found to be a unstable phase at a particular depth, the water is moved instantaneously upward, until it reaches a rock which assimilates water (Gerya et al., 2006). To formulate this method analytically we compute the velocity of water from the local kinematic transport condition.

$$v_{x(\text{water})} = v_x, \quad v_{z(\text{water})} = v_z - v_{z(\text{percolation})} \tag{A7}$$

Table A3
Model rock compositions (wt%)

	Sediment	Upper oceanic crust (altered basalt)	Lower oceanic crust (gabbro)	Mantle (peridotite)
SiO_2	61.10	47.62	53.49	45.55
Al_2O_3	12.43	14.48	14.07	4.03
FeO	5.43	10.41	6.86	7.47
MgO	2.59	6.92	12.07	37.42
CaO	6.21	13.39	10.73	3.18
Na_2O	2.54	2.15	1.22	0.33
K_2O	2.13	0.58	0.09	0.03
H_2O[a]	7.60	2.78	1.47	1.98

Sediment is the GLOSS average (Plank and Langmuir, 1998); basalt is an average for the upper 500 m of the igneous section of the oceanic crust (Staudigel et al., 1989); gabbro is a synthetic composition for the gabbroic section of the oceanic crust (Behn and Kelemen, 2003), modified to contain up to 1.5 wt% water to represent the effects of lower crustal hydrothermal alteration (Carlson, 2001), and peridotite is the LOSIMAG composition (Morris and Hart, 1986) chosen to represent mantle peridotite. The compositions have been simplified by the omission of minor elements such as Mn, P, Ti, and Cr and the assumption that all Fe is ferrous, additionally CO_2 has been removed from the GLOSS sediment composition.

[a] Maximal H_2O content in the rocks (cf. Section A3 for details of water balance at elevated *P* and *T*).

where v_x and v_z are local velocity of the mantle and $v_{z(\mathrm{percolation})}$ is the constant relative velocity of upward percolation of water through the mantle which was varied in different numerical experiments (Table 1).

In addition to water-bearing minerals at shallow depth (<50 km), free water is present in basaltic crust and sediments. Pore water content $x_{\mathrm{H_2O(p)}}$ is assumed to decrease linearly with depth as:

$$x(\mathrm{wt\%}) = (1 - 0.02\Delta z)x_{\mathrm{H_2O(p)}} \tag{A8}$$

where $x_{\mathrm{H_2O(p)}} = 2\,\mathrm{wt\%}$ is the water content at the surface and Δz is the depth in kilometer below the surface.

References

Arcay, D., Trie, E., Doin, M.P., 2005. Numerical simulations of subduction zones: Effect of slab dehydration on the mantle wedge dynamics. Phys. Earth Planet. Interiors 149, 133–153.

Bangs, N.L., Cande, S.C., 1997. Episodic development of a convergent margin inferred from structures and processes along the southern Chile margin. Tectonics 16, 489–503.

Behn, M.D., Kelemen, P.B., 2003. Relationship between seismic P-wave velocity and the composition of anhydrous igneous and meta-igneous rocks. Geochem. Geophys. Geosyst. 4, prt. no. 1041.

Burg, J.P., Gerya, T.V., 2005. The role of viscous heating in Barrovian metamorphism of collisional orogens: thermomechanical models and application to the Lepontine Dome in the Central Alps. J. Metamorph. Geol. 23, 75–95.

Carlson, R.L., 2001. The abundance of ultramafic rocks in Atlantic Ocean crust. Geophys. J. Int. 144, 37–48.

Chase, C.G., 1978. Extension behind island arcs and motions relative to hot spots. J. Geophys. Res. 83, 5385–5387.

Connolly, J.A.D., 2005. Computation of phase equilibria by linear programming: A tool for geodynamic modeling and its application to subduction zone decarbonation. Earth Planet. Sci. Lett. 236, 524–541.

Connolly, J.A.D., Petrini, K., 2002. An automated strategy for calculation of phase diagram sections and retrieval of rock properties as a function of physical conditions. J. Metamorphic Geol. 20, 697–708.

Connolly, J.A.D., Trommsdorff, V., 1991. Petrogenetic grids for metacarbonate rocks–pressure–temperature phase-diagram projection for mixed-volatile systems. Contribut. Mineral. Petrol. 108, 93–105.

Connolly, J.A.D., Kerrick, D.M., 2002. Metamorphic controls on seismic velocity of subducted oceanic crust at 100-250 km depth. Earth Planet. Sc. Lett. 204, 61–74.

Davies, J.H., 1999. The role of hydraulic fractures in generating intermediate depth earthquakes and subduction zone magmatism. Nature 398, 142–145.

Davies, J.H., Stevenson, D.J., 1992. Physical model of source region of subduction zone volcanics. J. Geophys. Res. Solid Earth 97, 2037–2070.

Enns, A., Becker, T.W., Schmeling, H., 2005. The dynamics of subduction and trench migration for viscosity stratification. Geophys. J. Int. 160, 761–775.

Ewart, A., Collerson, K.D., Regelous, M., Wendt, J.I., Niu, Y., 1998. Geochemical evolution within the Tonga-Kermadec Lau arc back-arc systems: the role of varying mantle wedge composition in space and time. J. Petrol. 39, 331–368.

Gerya, T.V., Burg, J.P., 2007. Intrusion of ultramafic magmatic bodies into the continental crust: Numerical simulation. Phys. Earth Planet. Interiors 160, 124–142.

Gerya, T.V., Connolly, J.A.D., Yuen, D.A., Gorczyk, W., Capel, A.M., 2006. Seismic implications of mantle wedge plumes. Phys. Earth Planet. Interiors 156, 59–74.

Gerya, T.V., Stockhert, B., Perchuk, A.L., 2002. Exhumation of high-pressure metamorphic rocks in a subduction channel: A numerical simulation. Tectonics, 21.

Gerya, T.V., Yuen, D.A., 2003a. Characteristics-based marker-in-cell method with conservative finite-differences schemes for modeling geological flows with strongly variable transport properties. Phys. Earth Planet. Interiors 140, 295–320.

Gerya, T.V., Yuen, D.A., 2003b. Rayleigh–Taylor instabilities from hydration and melting propel cold plumes at subduction zones. Earth Planet. Sci. Lett. 212, 47–62.

Ghiorso, M.S., Hirschmann, M.M., Reiners, P.W., Kress, V.C., 2002. The pMELTS: A revision of MELTS for improved calculation of phase relations and major element partitioning related to partial melting of the mantle to 3 GPa. Geochem. Geophys. Geosyst. 3, Prt. no. 1030.

Glodny, J., Lohrmann, J., Echtler, H., Grafe, K., Seifert, W., Collao, S., Figueroa, O., 2005. Internal dynamics of a paleoaccretionary wedge: insights from combined isotope tectonochronology and sandbox modelling of the South-Central Chilean forearc. Earth Planet. Sci. Lett. 231, 23–39.

Gorczyk, W., Gerya, T.V., Connolly, J.A.D., Yuen, D.A., Rudolph, M., 2006. Large-scale rigid-body rotation in the mantle wedge and its implications for seismic tomography. Geochem. Geophys. Geosyst., 7.

Gutscher, M.A., Kukowski, N., Malavieille, J., Lallemand, S., 1998. Material transfer in accretionary wedges from analysis of a systematic series of analog experiments. J. Struct. Geol. 20, 407–416.

Hasegawa, A., Zhao, D.P., Hori, S., Yamamoto, A., Horiuchi, S., 1991. Deep-structure of the Northeastern Japan Arc and its relationship to seismic and volcanic activity. Nature 352, 683–689.

Herveĭ, F, Demant, A, Ramos, V.A., Pankhurst, R.J., Suaĭrez, M., 2000. The southern Andes. In: Cordani, U.G., Milani, E.J., Thomaz Filho, A., Campos, D.A. (Eds.), Tectonic evolution of SouthAmerica. 31st International Geological Congress, pp. 605–634.

Hervé, F., Munizaga, F., Parada, M.A., Brook, M., Pankhurst, R.J., Snelling, N.J., Drake, R., 1988. Granitoids of the coastal range of central Chile:geochronology and geologic setting. J. South Am. Earth Sci. 1, 185–194.

Holland, T., Baker, J., Powell, R., 1998. Mixing properties and activity-composition relationships of chlorites in the system MgO-FeO-Al_2O_3–SiO_2–H_2O. Eur. J. Mineral. 10, 395–406.

Holland, T., Powell, R., 1996. Thermodynamics of order-disorder in minerals. 2. Symmetric formalism applied to solid solutions. Am. Mineral. 81, 1425–1437.

Holland, T.J.B., Powell, R., 1998. An internally consistent thermodynamic data set for phases of petrological interest. J. Metamorphic Geol. 16, 309–343.

Iwamori, H., Richardson, C., Maruyama, S., 2007. Numerical modeling of thermal structure, circulation of H_2O, and magmatism-metamorphism in subduction zones: implications for evolution of arcs. Gondwana Res. 11, 109–119.

Kelley, K.A., Plank, T., Grove, T.L., Stolper, E.M., Newman, S., Hauri, E., 2006. Mantle melting as a function of water content beneath back-arc basins. J. Geophys. Res., 111.

Kerrick, D.M., Connolly, J.A.D., 2002. Quantification of subduction zone metamorphic devolatilization from computed high pressure phase equilibria. Geochim. Cosmochim. Acta 66, A396.

Kukowski, N., Lallemand, S.E., Malavieille, J., Gutscher, M.A., Reston, T.J., 2002. Mechanical decoupling and basal duplex formation observed in sandbox experiments with application to the Western Mediterranean Ridge accretionary complex. Marine Geol. 186, 29–42.

Lucassen, F., Trumbull, R., Franz, G., Creixell, C., Vasquez, P., Romer, R.L., Figueroa, O., 2004. Distinguishing crustal recycling and juvenile additions at active continental margins: the Paleozoic to recent compositional evolution of the Chilean Pacific margin (36–41(circle)S). J. South Am. Earth Sci. 17, 103–119.

Miller, D.M., Goldstein, S.L., Langmuir, C.H., 1994. Cerium lead and lead-isotope ratios in arc magmas and the enrichment of lead in the continents. Nature 368, 514–520.

Morris, J.D., Hart, S.R., 1986. Isotopic and incompatible element constraints on the genesis of island-arc volcanics from Cold Bay and Amak Island, Aleutians, and implications for mantle structure—reply. Geochim. Cosmochim. Acta 50, 483–487.

Morris, J.D., Leeman, W.P., Tera, F., 1990. The subducted component in Island-Arc Lavas—constraints from Be isotopes and B-Be systematics. Nature 344, 31–36.

Newton, R.C., Charlu, T.V., Kleppa, O.J., 1980. Thermochemistry of the high structural state plagioclases. Geochem. Cosmochim. Acta 44, 933–941.

Pinkerton, H., Stevenson, R.J., 1992. Methods of determining the rheological properties of magmas at subliquidus temperatures. J. Volcanol. Geotherm. Res. 53, 47–66.

Plank, T., Langmuir, C.H., 1998. The chemical composition of subducting sediment and its consequences for the crust and mantle. Chem. Geol. 145, 325–394.

Poli, S., Schmidt, M.W., 2002. Petrology of subducted slabs. Ann. Rev. Earth Planet. Sci. 30, 207–235.

Ramos, V.A., Kay, V.M., 1991. Triassic rifting and associated basalts in the Cuyo basin, central Argentina. In: Harmon, R.S., Rapela, C.W. (Eds.), Andean magmatism and its tectonic setting, Geol. Soc. Amer. Spec. Paper 265, 79-91.

Ranalli, G., 1995. Rheology of the Earth. Chapman and Hall, London, 413 p.

Regenauer-Lieb, K., Yuen, D.A., Branlund, J., 2001. The initiation of subduction: Criticality by addition of water? Science 294, 578–580.

Rose, E.F., Shimizu, N., Layne, G.D., Grove, T.L., 2001. Melt production beneath Mt. Shasta from boron data in primitive melt inclusions. Science 293, 281–283.

Rupke, L.H., Morgan, J.P., Hort, M., Connolly, J.A.D., 2004. Serpentine and the subduction zone water cycle. Earth Planet. Sci. Lett. 223, 17–34.

Schellart, W.P., Freeman, J., Stegman, D.R., Moresi, L., May, D., 2007. Evolution and diversity of subduction zones controlled by slab width. Nature 446, 308–311.

Schmidt, M.W., Poli, S., 1998. Experimentally based water budgets for dehydrating slabs and consequences for arc magma generation. Earth Planet. Sci. Lett. 163, 361–379.

Sobolev, S.V., Babeyko, A.Y., 2005. What drives orogeny in the Andes? Geology 33, 617–620.

Staudigel, H., Hart, S., Schmincke, H., Smith, B., 1989. Cretaceous ocean crust at DSDP sites 417–418: Carbon uptake from weathering versus loss by magmatic outgassing. Geochim. Cosmochim. Acta 53, 3091–3094.

Stern, R.J., 2002. Subduction zones. Rev. Geophys., 40.

Takahashi, E., Kushiro, I., 1983. Melting of a dry peridotite at high-pressures and basalt magma genesis. Am. Mineralog. 68, 859–879.

Tatsumi, Y., 1986. Formation of the volcanic front in subduction zones. Geophys. Res. Lett. 13, 717–720.

Thompson, J.B., Hovis, G.L., 1979. Entropy of mixing in sanidine. Am. Mineralog. 64, 57–65.

Thomson, S.N., Hervé, F., 2002. New time constraints for the age of metamorphism at the ancestral Pacific Gondwana margin of southern Chile (42–52°S). Revista Geologica De Chile 29, 255–271.

Turcotte, D.L., Schubert, G., 2002. Geodynamics. Cambridge University Press, Cambridge, 456 p.

Uyeda, S., Kanamori, H., 1979. Back-arc opening and the mode of subduction. J. Geophys. Res. 84, 1049–1061.

van Hunen, J., van den Berg, A.P., Vlaar, N.J., 2002. On the role of subducting oceanic plateaus in the development of shallow flat subduction. Tectonophysics 352, 317–333.

Wei, C.J., Powell, R., 2003. Phase relations in high-pressure metapelites in the system KFMASH (K_2O–FeO–MgO–$A1_2O_3$–SiO_2–H_2O) with application to natural rocks. Contribut. Mine-Ralogy Petrol. 145, 301–315.

White, R.W., Powell, R., Phillips, G.N., 2003. A mineral equilibria study of the hydrothermal alteration in mafic greenschist facies rocks at Kalgoorlie, Western Australia. J. Metamorphic Geol. 21, 455–468.

Willner, A.P., Glodny, J., Gerya, T.V., Godoy, E., Massonne, H., 2004. A counterclockwise PTt path of high-pressure/low-temperature rocks from the Coastal Cordillera accretionary complex of south-central Chile: constraints for the earliest stage of subduction mass flow. Lithos 75, 283–310.

Willner, A.P., Thomson, S.N., Kroner, A., Wartho, J.A., Wijbrans, J.R., Hervé, F., 2005. Time markers for the evolution and exhumation history of a Late Palaeozoic paired metamorphic belt in north-central Chile (34 degrees-35 degrees 30′S). J. Petrol. 46, 1835–1858.

Wilson, T.J., 1991. Transition from back-arc to foreland basin development in the Southernmost Andes—stratigraphic record from the Ultima-Esperanza-District, Chile. Geol. Soc. Am. Bull. 103, 98–111.